On a radiolytic origin of red organics at the surface of the Arrokoth Trans-Neptunian Object

Eric Quirico, Aurore Bacmann, Cédric Wolters, Basile Augé, Laurène Flandinet, Thibault Launois, John Cooper, Véronique Vuitton, Thomas Gautier, Lora Jovanovic, et al.

Journal Pre-proof

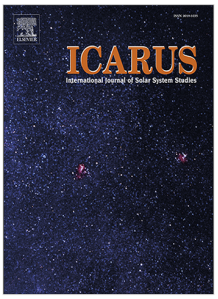

On a radiolytic origin of red organics at the surface of the Arrokoth Trans-Neptunian Object

Eric Quirico, Aurore Bacmann, Cédric Wolters, Basile Augé, Laurène Flandinet, Thibault Launois, John F. Cooper, Véronique Vuitton, Thomas Gautier, Lora Jovanovic, Philippe Boduch, Hermann Rothard, Léopold Desage, Alexandre Faure, Bernard Schmitt, Olivier Poch, William M. Grundy, Silvia Protopapa, Sonia Fornasier, Dale P. Cruikshank, S. Alan Stern, The New Horizons Team

PII: S0019-1035(22)00488-2
DOI: https://doi.org/10.1016/j.icarus.2022.115396
Reference: YICAR 115396

To appear in: *Icarus*

Received date : 30 June 2022
Revised date : 30 November 2022
Accepted date : 7 December 2022

Please cite this article as: E. Quirico, A. Bacmann, C. Wolters et al., On a radiolytic origin of red organics at the surface of the Arrokoth Trans-Neptunian Object. *Icarus* (2022), doi: https://doi.org/10.1016/j.icarus.2022.115396.

Highlights

On a radiolytic origin of red organics at the surface of the Arrokoth Trans-Neptunian Object

Eric Quirico,Aurore Bacmann,Cédric Wolters,Basile Augé, Laurène Flandinet,Thibault Launois, John F. Cooper,Véronique Vuitton,Thomas Gautier, Lora Jovanovic, Philippe Boduch, Hermann Rothard, Léopold Desage, Alexandre Faure, Bernard Schmitt, Olivier Poch, William M. Grundy, Silvia Protopapa,Sonia Fornasier,Dale P. Cruikshank,S. Alan Stern, The New Horizons Team

- The origin of Arrokoth's red surface through methanol ice radiolysis was investigated.
- Doses and destruction yields of methanol were calculated for Solar and Cosmic-rays ions.
- Experiments driven by calculations show that abundant red organics materials are synthesized in the first meter of the subsurface.
- These complex organics are composed of tens of thousands of individual molecules and cover a broad range of weight.
- A radiolytic origin of Arrokoth's red surface is plausible, provided the lack of major ablation event (e.g. collision in the Kuiper Belt).

On a radiolytic origin of red organics at the surface of the Arrokoth Trans-Neptunian Object

Eric Quirico[a,*], Aurore Bacmann[a], Cédric Wolters[a], Basile Augé[a], Laurène Flandinet[a], Thibault Launois[a], John F. Cooper[b], Véronique Vuitton[a], Thomas Gautier[c,g], Lora Jovanovic[c], Philippe Boduch[d], Hermann Rothard[d], Léopold Desage[a], Alexandre Faure[a], Bernard Schmitt[a], Olivier Poch[a], William M. Grundy[e], Silvia Protopapa[f], Sonia Fornasier[g,h], Dale P. Cruikshank[i], S. Alan Stern[f] and The New Horizons Team

[a]*Université Grenoble Alpes, CNRS, Institut de Planetologie et Astrophysique de Grenoble (IPAG), UMR 5274, , Grenoble, F-38041, France*
[b]*NASA Goddard Space Flight Center (Emeritus), , Greenbelt, MD 20771, Maryland, United States of America*
[c]*CNRS/INSU, LATMOS-IPSL, , Guyancourt, F-78280, France*
[d]*Centre de Recherche sur les Ions, les Matériaux et la Photonique, CIMAP-CIRIL-GANIL, Normandie Université, ENSICAEN, UNICAEN, CEA, CNRS, , Caen, 14000, France*
[e]*Lowell Observatory, Northern Arizona University, , Flagstaff, AZ86001, Arizona, United States of America*
[f]*Southwest Research Institute, , Boulder, CO 80302, Colorado, United States of America*
[g]*LESIA, Université Paris Cité, Observatoire de Paris, Université PSL, CNRS, Sorbonne Université, 5 place Jules Janssen, Meudon, 92195, France*
[h]*Institut Universitaire de France (IUF), 1 rue Descartes, Paris Cedex 05, 75231, France*
[h]*University of Central Florida. Dept of Physics., 4000 Central Florida Blvd, Orlando, FL 32816, USA*

ARTICLE INFO

Keywords:
Arrokoth
Trans-Neptunian Objects
Organics

ABSTRACT

The classical Kuiper Belt Object (KBO) Arrokoth was surveyed by the New Horizons spacecraft on 1st January 2019, revealing a small bilobed object with a red surface, whose spectral slope lies in the average of the whole KBOs population. This red color has been assigned to reddish organic materials, either inherited from the protosolar disk during accretion, or formed through radiolytic processes in the surface due to exposure to solar or interstellar photons, Solar Wind, Solar Energetic Particles or Galactic Cosmic Rays. We report here a study investigating the radiolytic scenario, based on numerical calculations and experimental simulations run with swift heavy ions (74.8 MeV $^{136}Xe^{19+}$ and 33.06 MeV $^{58}Ni^{9+}$), and low-energy 105 keV $^{18}O^{6+}$ ions on CH_3OH ice, the only molecule identified at Arrokoth's surface. Calculations show that sputtering is essentially controlled by Solar Wind (H and He), and that the sputtering rate depends on the nature of the material: erosion thickness over 4.55 Gyr are a few micrometers for amorphous carbon (as an analog of red organics) and a $\sim$ 240 μm to around $\sim$ 10 mm for H_2O and CO ice, respectively. Chemistry within the subsurface is essentially controlled by Galactic Cosmic rays (H and He), which penetrate deep down to several tens of meters and deliver an electronic dose higher than 1 eV.atom^{-1} in the first meter. The electronic and elastic doses delivered by Solar Wind ions are limited to the first 10s nm of the top surface, but Solar Energetic Particles deliver high electronic doses in the first 100 μm of the surface (up to 200 eV.atom^{-1}). Experimental simulations show that irradiating methanol ice with a dose consistent with that in planetary conditions, results in the formation of reddish organic materials made of aliphatic, conjugated and unconjugated olefinic, acetylinic, carbonyl and hydroxyl groups. A similarity with irradiated simple polymers (e.g. polyethyleneglycol) and materials formed through cold plasma experiments (tholins) is observed. There is little dependence with the nature and energy of the ion. The residue recovered at room temperature was analyzed with High Resolution Mass Spectrometry (Orbitrap), revealing a complex composition with around 6596 chemical formulas and likely several tens of thousands of molecules. Altogether, these analyses support active polymerisation mechanisms similar to those observed in irradiated polymers, as bond-breaking, cross-linking or formation of olefinic bonds through recombination of radicals in adjacent carbon atoms. Considering both sputtering and radiolysis, as well as material ablation due to dust bombardment reported in literature, a scenario is taking shape as the production of reddish organics deep in the subsurface, and the settling of an organic crust at the top surface through volatiles removal. The presence of methanol and absence of water, inconsistent with sputtering fractionation, remains unexplained.

*Corresponding author
eric.quirico@univ-grenoble-alpes.fr (E. Quirico)
ORCID(s):

1. Introduction

The Trans-Neptunian Object (TNO) Arrokoth was surveyed by the New Horizons spacecraft on 1st January 2019 (Stern et al., 2019). This small cold classical[1] Kuiper Belt Object (KBO) ∼ 33 km across has a bilobed shape, and consists of two rounded icy planetesimals (r ∼ 9.7 and 7.1 km). Reflectance spectra and spectro-photometric data collected by the LEISA and MVIC components of the Ralph instrument have revealed a reddish surface (Reuter et al., 2008; Grundy et al., 2020), as observed for a large fraction of the whole population of classical KBOs (Cruikshank et al., 2005; Barucci et al., 2005; Doressoundiram et al., 2008; Perna et al., 2010; Brown, 2012; Lacerda et al., 2014). Methanol has been identified, while no other ices were detected. The red material at Arrokoth surface has possibly two origins: (1) a primordial origin, i.e. formed in the proto-solar disk and accreted with the other constituents that form Arrokoth; (2) a radiolytic origin, as the airless Arrokoth is directly exposed to energetic radiations: Solar and interstellar photons, Solar Wind (SW), Solar Energetic Particles (SEPs) and Galactic Cosmic Rays (GCRs). The penetration of UV photons is very shallow (few hundreds of nm), with limited impacts on optical effects. In contrast, ions penetrate deeper in the subsurface, trigger chemistry and sputtering, and several experimental simulations have reported the formation of reddish organic materials from simple ices (Moore et al., 1996; Brunetto et al., 2006; Dartois et al., 2013; Materese et al., 2015; Auge et al., 2016, 2019; Urso et al., 2020b). However, the nature of the organic species formed in these experiments remains poorly known, and the experimental doses are not necessarily in agreement with the actual conditions at the surface and in the subsurface of Arrokoth.

In this study, our objective is to question a radiolytic origin of the red color of Arrokoth through numerical simulations and ion irradiation experiments. We report numerical simulations that estimate the sputtering rate of a surface composed of pure methanol ice, the elastic and electronic doses and the destruction yield of methanol upon depth in the subsurface (section 2). We present in a second step (section 3, 4) the results of ion irradiation of methanol ice that were conducted under conditions that fit with estimates provided by calculations. The organic byproducts were characterized by Visible and IR spectroscopy, and the room temperature residue was investigated by High Resolution Mass Spectrometry (HRMS). These results are finally discussed (section 5) in the general astrophysical context of Arrokoth, leading to the conclusion that reddish materials should be present in Arrokoth conditions through a radiolysis chemistry controlled by GCRs, provided that the first meters of the surface were not removed by dust ablation or collisions within the Kuiper Belt.

2. Energetic particles at Arrokoth's surface

In this section, we provide estimates of (1) the erosion thickness controlled by sputtering and (2) the electronic and nuclear doses deposed versus depth in a methanol putative surface. The electronic and nuclear irradiation doses are a global indicator of the energy made available for chemistry in an irradiated solid, and a simple proxy for comparison with experimental data presented in the next section.

2.1. Sputtering

We first consider the sputtering effect of SW and GCR for species present on a semi-infinite surface. In that case, neglecting radiolysis chemistry during the process, the column density N (molec.cm^{-2} or at.cm^{-2}) of a molecule or atom sputtered by an ion X with an energy E reads:

$$\frac{dN}{dF} = -Y_X(E) \tag{1}$$

where F is the fluence (ions.cm^{-2}) and Y_X (molec.ion^{-1} or at.ion^{-1}) the sputtering yield. This column density corresponds to the erosion thickness t:

$$t = C\frac{M}{\rho N_a}\Delta t \sum_{i=1}^{92}\int_{E_{min}}^{E_{max}} Y_X^i(E)\left(\frac{dN}{dE}\right)_i dE \tag{2}$$

[1] cold classical: small objects on low inclination and low eccentricity orbits, over heliocentric distances between 42 and 47 au.

where M is the molar mass, Δt the irradiation time, ρ the density, N_a the Avogadro number, i the atomic number of the chemical element, and $\left(\frac{dN}{dE}\right)_i$ the ions differential flux at energy E. The angular dependency of the sputtering yield is neglected and the value at normal incidence is used. The density of crystalline methanol ice $\rho = 1.02$ g.cm^{-3} was taken from Torrie et al. (1989). Our calculations were limited to the most abundant elements H, He, C, N, O, Mg, Si and Fe. In the case of GCR, which is omnidirectional and isotropic, C=π, resulting from the average over all incidences from 0 to 90 ° for the co-latitude angle and 0 to 180 ° for the azimuthal angle.

The case of SW is more complicated and needs assumptions and simplifications. Arrokoth's obliquity is 99°, close to $\pi/2$, which means that the surface is in average uniformly irradiated during half of an orbital period. Therefore, the irradiation time over 4.55 Gyr was taken as 2.225 Gyr. We have assumed that SW is directional and hits a smooth and flat Arrokoth's surface, and only consider the surface perpendicular to the rotation vector. As the angle of the incoming SW with respect to the surface varied between 0 and $\pi/2$, the averaged irradiation flux equals the flux at θ=0 (θ being the incidence angle with respect to the normal vector at the surface) multiplied by the averaged cosine $\overline{cos\theta}=2/\pi$. As the flux density is given per steradian, we multiply by π, assuming an isotropic flux density over an hemisphere, which overestimates the actual value. Finally, this leads to C=2.

Two SW/SEPs differential fluxes were used. First, we used the He fluence measured at 1 au between 10/97 and 06/00 by Mewaldt et al. (2007), assuming a simple scaling law with the solar abundances of Meyer et al. (1998). The differential flux at 44 au was obtained by applying a $1/44^2$ factor (Fig. 1). This scaling appears consistent with the $\sim 1/R^2$ dependance (R being the heliocentric distance) of the proton density and energy flux (Liu et al., 2021; Adhikari et al., 2015). However, it neglects interstellar pickup ions and cooling of the bulk plasma temperature, which results as a narrowing of the SW peak at $\sim$ 1 keV/u. In this respect, we used for comparison a differential protons flux modelled from the LECP (Voyager 1 and 2) and PEPSSI (New Horizons) instruments (Fig. 1). The contribution of the slow and fast SW and SEPs (E > 10 keV/u) are processed as two distinct sources in some publications (Urso et al., 2020a). Here, the differential fluxes used span the range 1 x 10^{-4} - 30 MeV/u and include both of them. However, the quiet Sun conditions that prevailed in the period 10/1997 to 06/2000 have been extrapolated to 4.55 Gyr. This assumption does not hold in the first millions of years of the very active young Sun, which could have been 100-1000 times more active in terms of mass loss. Unfortunately, young Sun SW/SEPs fluxes are basically unknown due to the lack of compelling direct detection of stellar wind around solar-type stars, and poorly reliable indirect estimates (Ribas et al., 2005).

The contribution of GCR ions to sputtering was estimated using the differential flux of Webber & Yushak (1983). This differential flux, in atom.cm^{-2}.s^{-1}.sr^{-1}.(MeV)$^{-1}$, was established for protons in Local Interstellar Medium and is easy to compute using the following parametric equation:

$$\frac{dN}{dE} = \frac{CE^{0.3}}{(E+E_0)^{0.3}} \tag{3}$$

with C=9.42 x 10^4 and E_0 a form parameter related to solar modulation, set to 400 MeV to fit Voyager 1 protons measurements (Stone et al., 2013; Cummings et al., 2016) (Fig. 1). For other chemical elements, a scaling law of the cosmic abundance was applied and the C and the E_0 parameters were tuned to fit Voyager 1 data (Cummings et al., 2016) (Tab. 1). Last, but not least, the GCR flux at 44 au is not similar to that in LISM, due to the heliospheric shielding (Usoskin et al., 2005). Measurements at 40 au are only available for protons (Cooper et al., 2003), therefore sputtering calculations have been run using the LISM differential fluxes to consider separately the contribution of each element, thereby overestimating the erosion thickness.

Arrokoth's surface and subsurface are possibly made of several ices and organic materials, but to date only methanol has been identified by the New Horizons spacecraft (Grundy et al., 2020). In addition, its composition could have evolved along 4.55 Gyr. We therefore focused on three case models for which sputtering yields were available at low energy: (1) CO ice, (2) H_2O ice, as the most and less volatile molecules in the icy component of the surface, and (3) amorphous carbon as a simulant of putative reddish organics dispersed in the surface materials. Note that pure CO ice is not expected to be present at the surface of Arrokoth, due to its surface temperature, and is used here to provide an upper limit of surface sputtering. The case of methanol ice could not be considered, due to the scarcity of sputtering yields available in literature. Amorphous carbons constitute a broad family of disordered solids, which are classified according to their elemental composition (H/C, N/C), sp^3/sp^2 ratio and optical properties (e.g. Tauc or E_{04} gaps) (Ferrari & Robertson, 2000). As there is a limited number of sputtering yields published to date, we had to

Table 1
C and E_0 parameters of the Webber and Yushak (1983) parametric equation that fit Voyager 1 data with A_i chemical element abundances.

Element	C	E_0	A_i [1]
H	9.42×10^4	400	1
He	5.5×10^5	700	8.14×10^{-2}
C	8.5×10^4	800	1.67×10^{-3}
N	1.3×10^5	850	2.44×10^{-4}
O	1.4×10^5	750	1.57×10^{-3}
Mg	2.0×10^5	600	2.26×10^{-2}
Si	2.0×10^5	600	1.90×10^{-4}
Fe	2.0×10^5	600	1.11×10^{-4}

[1] Cummings et al. (2016)

compile data collected on different types of amorphous carbons, and calculate sputtering yields at low energy through Monte-Carlo simulations (SRIM software; http://www.srim.org/).

2.1.1. CO ice

The sputtering yield of CO ice Y_{CO} follows a S_e^2 dependance (S_e being the electronic stopping power) for irradiation events dominated by electronic interactions (Brown et al., 1984; Seperuelo Duarte et al., 2010). However, at low energy in the solar wind peak, elastic interactions and cascade recoils significantly contribute to sputtering (Sigmund, 1969). Balaji et al. (1995) measured sputtering yields of CO ice irradiated with He^+, Ne^+, Ar^+ and Kr^+ ions in the range 1-5 keV. Chrisey et al. (1990) focused on He ions in the range 10-60 keV, and Schou & Pedrys (2001) report sputtering yields of protons in the range 9-60 keV. We observe that in the case of H and He irradiations, dominated by electronic interactions, there is no good match between these studies and values obtained from Brown et al. (1984) and Seperuelo Duarte et al. (2010). Reproducibility is a challenging issue, as sputtering yields are very sensitive to film thickness, surface morphology or sample ageing. Note, for instance, that the data of Chrisey et al. (1990) have been rescaled by Schou & Pedrys (2001), and, here, we have used these rescaled data. H seems a particular case as its sputtering yield seems to follow a $E^{1.3}$ dependency with S_e (Schou & Pedrys, 2001), as observed in the case of H_2O ice by Shi et al. (1995).

For our calculations, we have combined the low energy data of Schou & Pedrys (2001) and Balaji et al. (1995) with those from Brown et al. (1984) and Seperuelo Duarte et al. (2010). The sputtering yield value at the high-energy edge of the low-energy data of Schou & Pedrys (2001) and Balaji et al. (1995) was extrapolated at higher energy until it meets the sputtering yield of Seperuelo Duarte et al. (2010). This extrapolation certainly results in an overestimation of the actual sputtering yield in this energy range. In the case of protons, no data exist in the SW energy range, we therefore extrapolated the low energy values of Schou & Pedrys (2001) towards low and high energy, resulting once again in an overestimation of the role of protons. Finally, for estimating the erosion thickness of the C, N, O, Mg, Si and Fe ions, we made the following approximations: $Y_{CO}[C] \simeq Y_{CO}[N] \simeq Y_{CO}[O] \simeq Y_{CO}[Ne]$; $Y_{CO}[Mg] \simeq Y_{CO}[Si] \simeq Y_{CO}[Ar]$; and $Y_{CO}[Fe] \simeq Y_{CO}[Kr]$.

Results on SW erosion are tabulated in Table 2. We first observe that the erosion thicknesses calculated with the modelled SW/SEPs flux distribution are lower by around a factor of ten compared to the differential flux extrapolated from the measurements of Mewaldt et al. (2007). We hereafter focus on the results obtained with the modelled differential flux. The most contributing ion to erosion thickness is H (6 mm), followed by O, He and Fe, and the total erosion thickness is $\sim$ 10 mm. This upper limit value is significant, but it is unlikely it was achieved in real conditions. First because CO molecules were likely mixed up with other polar species, lowering their sublimation temperature and thereby their sputtering yield, and second because we have severely overestimated H sputtering yields. For GCR surface erosion, calculations run for H, He and Fe provide erosion thicknesses of 6.8×10^{-3}, 6.9×10^{-3} and 0.55 μm, respectively, for an irradiation time of 4.55×10^9 yr. The actual values are lower, because the GCR density flux is expected lower at 44 au (Cooper et al., 2003). In any case they are very weak, and by far the contribution of GCR to surface sputtering is negligible with respect to SW/SEPs.

Table 2
Solar Wind erosion thickness of CO, H_2O and a-C surfaces at 44 au over 4.55 Gyr

	Thickness (μm)					
	CO ice		**H_2O ice**		**a-C**	
	[1]Mewaldt @ 1au/44[2]	[2]Model	Mewaldt @ 1au/44[2]	Model	Mewaldt @ 1au/44[2]	Model
H	54889	6216	1400	168	16.1	1.9
He	11712	1261	254	29	9.3	1.1
C	6536	758	85	0.9	0.9	0.10
N	299	35	5	0.5	0.02	0.002
O	8105	939	142	14	0.7	0.09
Mg	1894	222	24	2.6	0.6	0.06
Si	1824	214	22	2.4	0.6	0.07
Fe	3412	402	126	12	0.8	0.1
Total	**88671**	**10047**	**2058**	**237**	**29.0**	**3.35**

[1]Using SW/SEPs differential flux from Mewaldt et al. (2007) at 1 au rescaled at 44 au by applying a factor $1/44^2$. [2]Using SW/SEPs differential flux estimated from modelling (see Text).

2.1.2. H_2O ice

The sputtering yield of water ice at E < 50 keV/u was calculated with the parametric equation of Fama et al. (2008), and at higher energies the sputtering yields of Brown et al. (1984) and Dartois et al. (2015) were used (Fig. 2). There is no good match between the two sets of data, except for H (which is unexpected due the non quadratic dependence with Se). Calculations show that the erosion thickness is 237 μm, and that H is the most contributing ion (168 μm).

2.1.3. Amorphous carbon

In the low energy range, the sputtering yields of amorphous carbon (C atom.ion^{-1}) have been estimated with the SRIM software for the H, He, C, N, O, Mg, Si, Fe elements at 0.5, 1, 5, 10, 50, 10 and 500 keV. The sputtering yield of each ion was then set to the highest of these values, and assumed to be constant up to high energies dominated by electronic interactions. Calculations were run for a H/C=0.5 carbon material, $\rho = 1.5$ g.cm^{-3}, displacement energy 5 eV, lattice binding energy 1 eV and surface binding energy 4 eV (values for sp^3-rich amorphous carbons, see Ullmann et al. (1993); Vukovic et al. (2018)). SRIM simulations provide values consistent within a factor of 2 with experimental measurements for a tetrahedral amorphous carbon (ta-C) irradiated with 50 keV Ga ions (Stanishevsky, 2001). At higher energies, experimental measurements are available, but display huge variabilities from a few tens to several 10^6 of C atom.ion^{-1} (Assmann et al., 1996; Behrisch et al., 1996; Boutard et al., 1989; Dollinger et al., 1996; Ghosh et al., 2002; Khan et al., 2013; Pawlak et al., 1999). H-bearing amorphous carbons seem to have a much higher sputtering yield than pure amorphous carbons, and we have selected the data from Pawlak et al. (1999) on a polymeric hydrogenated amorphous carbon (polymeric a-C:H). This kind of amorphous carbon resembles to the methanol ice residue produced in this study (see below), except for the presence of oxygen. The fit of Pawlak et al. (1999) data leads to $Y = -1303 + 1759 S_e$ (S_e in keV.nm^{-1}), which is different from the quadratic dependance observed for ices (for He and heavier ions). Note that irradiation leads to chemical fractionation and structural evolution of the film, and a decrease of sputtering yield over irradiation time. With all this in mind, the upper value of the erosion thickness is 3.35 μ m, around 2 order of magnitudes lower than water ice.

2.2. Electronic and nuclear doses

The electronic and nuclear doses (eV.atom^{-1}) deposited in the subsurface at a depth of z can be written as:

$$D^i_{e,n}(z) = C\frac{M}{6\rho N_a}\Delta t \sum_{j=0}^{89}\sum_{i=1}^{92}\int_{E_{min}}^{E_{max}} S^i_{e,n}(z,E)\times A_i\frac{dN}{dE}(d_j,E)dE \quad (4)$$

with z the vertical depth in the surface, d_j the distance between the ion entry point and the point at z where the dose is calculated (the ion incidence angle is $\theta_j = arcos(z/d_j) = j\pi/180$ and $j \in [0;89]$), M the molar mass, ρ

the density of methanol ice, N_a the Avogadro number, dN/dE the differential flux (SW or GCR), E_{min} and E_{max} the edges of the energy range, A_i the solar or LISM abundance of the i^{th} chemical element and Δt the irradiation duration (4.55 Gyr for GCR, 2.225 Gyr for SW). C=2 or π for SW and GCR, respectively. Power law grids were used for the depth and energy ranges, as $z_i = z_{min}(z_{max}/z_{min})^{i/N}$ (z_{min}:z_{max}=10^{-4} : 60 x 10^3 mm, GCR; =10^{-5}:5 mm, SW) and $E_i = E_{min}(E_{max}/E_{min})^{i/N}$ (E_{min}:E_{max}=10^{-2}:10^4 MeV/u, GCR; =3x10^{-4}:30 MeV/u, SW). The stopping powers S_e^i and S_n^i were calculated with the SRIM software for pure methanol ice, and the numerical code was computed with the software Igor Pro 8.04 (Wavemetrics). We have used the same differential fluxes and chemical elements that were used for sputtering calculations. Note the dose is given in eV/atom, i.e. we have calculated the dose for one methanol molecule, and divided it by 6.

The results are displayed in Figure 3 for Galactic Cosmic rays. Using the LISM differential flux, the total dose is > 10 eV.atom^{-1} until 1 m, and is in the range 1-10 eV.atom^{-1} until 10 m. The main contributors are H and He for $z < 1m$, and these two ions are the only ones penetrating above 1 m. At 40 au, we have run a calculation for protons using the differential flux of Cooper et al. (2003) (Fig. 3). The LISM electronic dose is 4.9-6.3 times larger than that at 40 au in the first 100 mm, and progressively reaches the 40 au values when increasing depth. We then infer that the actual total dose at 40 au lies around 10 eV.atom^{-1} in the first 10 mm, is higher than 1 eV.atom^{-1} in the first meter, and drops above. These calculations also show that the nuclear dose remains below 0.2 eV.atom^{-1}. It is worth noting that the penetration of GCR is much higher than the sputtering thickness controlled by SW/SEPs (237 μm for water ice and 3.35 μm for a-C).

In the case of SW and SEPs, sputtering and dose deposition upon depth need to be computed simultaneously, because the implantation depth is smaller than the erosion thickness. A time-resolved simulation was run over 2.25 Gyr with an incremental time of 222500 years (Fig. 4). For protons, calculations show that the layer that receives a > 10 eV.atom^{-1} nuclear dose is around 30 nm thick. This dose of 10 eV.atom^{-1} is the critical nuclear dose above which a carbonaceous material transforms into an amorphous carbon (Faure et al., 2021) for details. However, the electronic dose lies between 10 and 200 eV/atom in the first 100 μm, which are very high values.

3. Experimental methods

Experiments were conducted at Grand Accélérateur National d'Ions Lourds (GANIL, Caen, France) on the IRRSUD and ARIBE beamlines with the IGLIAS setup (Tab. 3; see Auge et al. (2018) for a detailed description). Infrared spectra were collected with a Bruker Vertex 70v FTIR spectrometer, operating with a MCT-detector and a 4 cm^{-1}and 1 cm^{-1}spectral resolution, for E1 and (E2, E3, E4), respectively. The angle between the spectrometer beam and the sample surface was 78 °. Thin films were deposited at normal incidence with a needle placed at around 15 mm from a MgF_2 or a ZnS window. The deposition rate was adjusted to get a good optical quality, and sample thickness was estimated using the band strengths of Bouilloud et al. (2015). The gaseous species sputtered in the chamber were detected with a MKS Microvision 2 quadrupole mass-spectrometer (QMS). IGLIAS is also equipped with a Perkin Elmer Lambda 650 VUV spectrometer, but the rapid degradation of the optical quality of the sample upon irradiation led to significant scattering that blurred the absorption signal.

High Resolution Mass Spectrometry analysis of the final organic residue was performed with an LTQ Orbitrap XL^{TM} mass spectrometer (Thermo Scientific, Bremen, Germany). This instrument is an hybrid mass spectrometer that uses an ion trap connected to an Orbitrap cell. The ion production was done with an IonMax^{TM} electrospray (ESI) source, which consists in a soft ionization achieved by protonation or deprotonation, respectively $[M+H]^+$ or $[M-H]^-$. All analyses were performed at the maximum instrument resolution (100000 at m/z = 400) for a mass accuracy of ± 2 ppm) using an Automatic Gain Control (AGC) set to 500000 ions storage. For accurate mass calibration, we used the commercial default LTQ-Orbitrap-XL instrument calibration mixture made of cafeine, Met-Arg-Phe-Ala peptide (MRFA), and Ultramark 1621 (a mixture of fluorinated phosphazine polymers) in positive mode, and a mixture of sodium dodecyl sulfate, sodium taurocholate and ultramark 1621 for negative mode.

Measurements were run with the following ESI source parameters, in positive and negative mode, respectively: 3.5 and -3.5 kV, Sheath gas at 3 and 10 (arb), capillary temperature at 275 °C and tension on the transfer tube at 40 and -35 V. Each measurements consisted of 3 scans of 256 microscans. The detailed description of the whole procedure can be found in Wolters et al. (2020).

The organic residue recovered at room temperature was solubilized through five washing with 250 μL of methanol (Carlo Erba, UPLC/MS grade) into a petri dish. The solution inside the petri-dish was transfered into a glass vial, and the petri-dish was washed again by adding 100 μL of methanol. This fraction was added to the previously recovered

solution in the glass vial. A procedural blank was made by washing the cleaned petri-dish with 2 x 250 μL of methanol and placed into a glass vial. Finally, the optical absorption of this solution was measured in the range 200-800 nm with a JASCO VUV V-730 spectrometer, and then analyzed by HRMS. Methanol was purchased from Sigma Aldrich (high purity, HPLC grade) and deuterated methanol was purchased from Eurisotop (purity 99.80 %).

4. Experimental results

We report a series of experiments on methanol ice run with different ions at different energies (Tab. 3). One experiment was run on deuterated methanol to easier the identification of simple by-products.

4.1. CH_3OH -$^{136}Xe^{19+}$ at 0.55 MeV/u

4.1.1. Spectroscopic monitoring

A CH_3OH film was deposited at 10 K and irradiated at normal incidence with 0.55 MeV/u $^{136}Xe^{19+}$ ions (E=74.8 MeV) (Fig. 5). At this temperature, solid methanol is amorphous and its density is sensitive to the deposition conditions (growing rate, beam collimation, angle with respect to the substrate). Luna et al. (2018) report a value of 0.664 g.cm^{-3} for methanol ice deposited at 10 K and 0.636 g.cm^{-3} at 20 K, while Hudson et al. (2020) report 0.779 g.cm^{-3} at 15 K. These studies also report different values for crystalline methanol ice: 1.02 against 0.795 at 120 K, for Hudson et al. (2020) and Luna et al. (2018), respectively. The value of Hudson et al. (2020) is similar to the value determined by neutron diffraction (Torrie et al., 1989), which would mean that perfectly stacked monocristalline solids were formed. However, this is unrealistic and the value of Luna et al. (2018) is more consistent with polycrystalline films hosting a significant porosity due to voids at grains boundary. Finally, regarding that amorphous films display a range of porosity, depending on experimental conditions, we used an average of both studies as 0.71 $\pm$ 0.072 g.cm^{-3} for calculating the doses deposited in the sample.

The maximum fluence was 8 x 10^{12} cm^{-2}, corresponding to an electronic dose D_e=5.9 eV.atom^{-1}. The column density and thickness of the film were estimated using the infrared integrated cross-section of the C-O band determined by Bouilloud et al. (2015) (integrated between 986 and 1070 cm^{-1}) (Tab. 3). The sputtered methanol thickness achieved for the maximum fluence of 8 x 10^{12} cm^{-2} was estimated to be 0.03-0.06 μm (against 10.8 μm for the initial thickness of the film), using the sputtering yield of Dartois et al. (2019) rescaled to the electronic stopping power of our experiment (assuming a quadratic dependence with the electronic stopping power). As a result, the radiolytic process mostly controls the decrease of the methanol ice film and there is no need to model sputtering. For the CO most volatile by-product, an estimate of the upper value of sputtered thickness lies around 0.4 μm, using the sputtering yield of pure CO ice from Seperuelo Duarte et al. (2010). The experiment was conducted in two steps: (1) the study of the film and the gaseous by-products during irradiation, until the maximum fluence of 8 x 10^{12} ions.cm^{-2}; (2) and during a Thermally Programmed Desorption (TPD) using a thermal ramp of 0.05 K.min^{-1}.

The spectra of the film during irradiation are displayed in Fig. 5. CO, CO_2, CH_4 and H_2CO are detected as the main simple by-products, consistently with previous studies (Moore et al., 1996; Brunetto et al., 2006). These species were also detected in the gas phase by the QMS spectrometer, plus H_2 and H_2O. H_2 is also a well known by-product that points to sample dehydrogenation. H_2O results from methanol radiolysis according to experiments run on CD_3OD (see below), however, a fraction could be due to contamination from the residual gas in the chamber. The infrared bands of the CH_3OH molecule decrease and broaden with increasing fluence, and above an electronic dose of 1.45 eV.at^{-1}, two broad congested organic bands arise between 1700 and 1300 cm^{-1}. At the maximum fluence, the spectrum of the film displays a slope and an asymmetry in the edges of the large 3500-3000 cm^{-1}OH band (Fig. 6), which points to significant scattering. Accordingly, we have considered that VUV absorption measurements collected during irradiation were blurred by significant and unquantified scattering.

During the TPD sequence, the film was progressively stripped from volatile species, until the formation of a refractory reddish organic residue at room temperature (Fig. 6). CO starts sublimating around 25 K and a large fraction is expelled from the film before 65 K. However, a few CO molecules remain until 130 K, pointing to CO binding interactions with polar hydroxyl groups (Kouchi, 1990). CH_4 and H_2CO are fully sublimated at 130 K, while CO_2 fully vanishes around 150 K. The organic bands in the region 1800-1200 cm^{-1}are almost unchanged below 130 K, and then progressively decrease until room temperature by a factor ranging from 2 to 6.5 (Fig. 6). Between 175 and 210 K, the shape of the OH band changes and displays 3 components that point to the presence of crystalline water ice, and the lack of C-O band around 1000 cm^{-1}shows that all CH_3OH has gone. These observations are confirmed by QMS measurements, which show, in addition, that methanol essentially sublimates between 125 and 155 K, H_2O

Table 3
Irradiation experiments parameters.

Experiment	T	Ion	E	F max	D_e max	S_e	D_n max	S_n	t	N	PR
	K		MeV	ions.cm^{-2}	eV.atom^{-1}	keV. μm^{-1}	eV.atom^{-1}	keV.μm^{-1}	nm	mol.cm^{-2}	nm
E_1 CH_3OH	10	$^{136}Xe^{19+}$	74.8	8 x 10^{12}	5.9	5934	0.047	49.5	10872	1.43 x 10^{19}	25875
E_2 CD_3OD	10	$^{58}Ni^{9+}$	33.1	1 x 10^{13}	4.4	3574	0.016	12.5	1270	1.70 x 10^{18}	21630
E_3 CH_3OH	40	$^{18}O^{6+}$	0.105	1.38 x 10^{15}	16.1	132	5.7	46.3	898	1.20 x 10^{18}	520
E_4 CH_3OH											
layer 1	40	$^{18}O^{6+}$	0.105	6.12 x 10^{14}	10.1	132	3.54	46.3	1512	2.00 x 10^{18}	
layer 2			0.105	1.57 x 10^{15}	25.9		9.07		1488		
layer 3			0.105	1.65 x 10^{15}	27.2		9.53		1335		
layer 4			0.105	1.70 x 10^{15}	28.0		9.82		1276		

T: temperature. E: total energy of the ion. F max: maximum fluence. De max: maximum electronic dose. Se: electronic stopping power. Dn: maximum nuclear dose. Sn: nuclear stopping power. t: thickness. N: CH_3OH column density. PR: projected range (penetration depth of the ion). The relative uncertainty on thickness and column density is estimated to 10 %. Se and Sn were calculated with SRIM for a density of 0.71 g.cm^{-3} for CH_3OH, and 0.80 g.cm^{-3} for CD_3OD. Note that for E1, there is a factor of 2 between the dose at the entry and exit of the sample, and the dose indicated in the table is therefore the dose accumulated in the uppermost layers of the sample. For experiments E3 and E4, the thickness is > PR, and ions implant into the sample. To optimize the thickness of the final irradiation residue, the sample was deposited in 4 steps, each consisting in depositing a layer followed by irradiation. Due to sputtering and to avoid further irradiation of the underlying film, the thickness of each film was larger than PR.

between 155 and 210 K, and that H_2CO has a narrow sublimation surge around 30 K (See Appendix B). Above 210 K, no peaks with significant intensity were detected, all ices have vanished and the infrared spectra are dominated by organic materials (Fig 7). Their spectra display:

(i) a broad feature between 2900 and 3600 cm^{-1}, due to the OH chemical group (B_{OH});

(ii) an aliphatic band between 2800 and 3000 cm^{-1}with peaks at 2958, 2933 and 2879 cm^{-1}, due to the symmetric and anti-symmetric stretching modes of CH_3 and CH_2 modes, the C-H stretching mode and complex vibrational interactions including Fermi resonance with the overtones of bending modes (MacPhail et al., 1984) ($B^s_{CH_x}$);

(iii) an asymmetric broad band between 1800 and 1500 cm^{-1}($B_{C=O,C}$), which comprises the stretching modes of C=O and C=C;

(iv) a broad band between 1500 and 1300 cm^{-1}($B^b_{CH_x}$), resulting from different vibration modes of CH_x groups, including bending.

We observe a global drop of band intensities when increasing temperature, i.e. a broad range of volatilities and of molecular weight. In spectra normalized at 1700 cm^{-1}, B_{OH}, $B^s_{CH_x}$ and $B^b_{CH_x}$ drop with increasing temperature, showing a decrease of the H/C and O/C elemental ratio, and thereby an increase of unsaturation. By the way, this confirms that $B^b_{CH_x}$ is essentially controlled by CH_x groups. The $B_{C=O,C}$ band is a very congested feature. It is controlled by the stretching modes of the carbonyl (C=O) and olefinic (C=C) chemical groups (Fig. 8). The C=O stretching component lies between 1670 and 1800 cm^{-1}and that of C=C between 1670 and 1600 cm^{-1}(Lin-Vien, 1991). Unconjugated C=C bonds, which do not lead to $\pi-\pi^*$ transitions in the visible (no colouring effect), lie between 1650-1670 cm^{-1}. C=C bonds conjugated with C=O lie between1650 and 1600 cm^{-1}, and C=C/C=C conjugation lie in the range 1640-1600 cm^{-1}. C=C conjugation also leads to a splitting of the stretching mode into symmetric and anti-symmetric components. Figure 8 shows a tentative spectral decomposition of the spectrum of the refractory residue. Regarding the lack of constraints on the actual number and position of the components, other solutions are possible and no unambiguous spectral decomposition can be achieved. Complicating the picture, the band strength of olefinic bonds or aromatic C=C are very sensitive to the molecular environment, in particular to the C=O group that has a strong dipolar moment (Painter et al., 1981).

The composition of the film after irradiation was estimated using the integrated absorption cross-sections from Bouilloud et al. (2015). The following column densities were found: N_{CO_2}= 1.59 x 10^{17}; N_{CO}= 2.10 x 10^{18}; N_{CH_3OH}=

2.68 x 10^{18}; N_{CH_4}= 3.20 x 10^{17}; N_{H_2CO}= 7.49 x 10^{17} molec.cm^{-2}. The column density of CH_2+CH_3 groups was calculated using the band strengths of the antisymetric stretching bands (Dartois et al., 2007), and was found to be 4.1 x 10^{17} molec.cm^{-2} for the spectra collected at 210 K during the TPD. The fraction of alkyl groups that sublimated below 210 K cannot be directly estimated because they are blurred by other bands, in particular the broad OH band. As a consequence, it was roughly estimated through the intensity of the ($B^b_{CH_x}$) band, which decreases by a factor of 2.7 between 40 and 210 K. Using the initial column density of CH_3OH N_{CH_3OH}=1.43 x 10^{19} molec.cm^{-2}, we estimate these species account for 50% of the starting carbon atoms, and CH_2+CH_3 groups represent 18% of these detected carbon atoms. However, we have not estimated the contribution of carbonyl and olefinic groups, due to the strong spectral congestion. In addition, aliphatic CH and non-protonated C have not been estimated. We then only estimate a lower value of $\sim$ 10% for initial carbon atoms incorporated in organic molecules. Beside the lack of detection of olefinic, carbonyl, non-protonated and C-H aliphatics, some small volatile species may have been undetected by FTIR (due to the lack of IR active vibrations) and by QMS data, due to a lack of precision in peak intensites and reference spectra. Another explanation is the quite large uncertainty on band strengths. Usually a relative error of 30% is given, but they can also be blurred by systematic errors (e.g. lack of knowledge about density). Last, spectral congestion and baseline correction are always an issue, and can lead to very significant systematic errors (i.e. H_2CO).

The residue recovered at room temperature was dissolved in methanol for analysis by VUV absorption spectroscopy (Fig. 9). The transmission spectrum of the solution shows an absorption continuum from the UV to $\sim$ 500 nm, consistent with the reddish colour observed by the naked eye. This information is semi-quantitative, as the nature of the species and their concentrations are unknown in the detail.

4.1.2. Molecular complexity of room-T residues

Mass spectra of the residue solubilized in methanol were collected along the procedure described in section 3. These spectra are complex in terms of peak numbers (several thousands). We have used here a homemade software developed at IPAG with the IGOR Pro software (Wavemetrics) (Orthous-Daunay et al., 2019). The data description was achieved in three successive steps: (1) the description of the mass spectrum, (2) the analysis of the apparent diversity and (3) the description of the attributed stoichiometric formulas. A mass spectrum contains much information simply derived from the mass and intensity of the peaks, such as intensity patterns and profiles, or systematic mass differences. Once the general data structure has been described, the stoichiometric diversity is analyzed through dedicated mathematical processing, which are allowed by the high precision and mass resolution of the Orbitrap spectrometer. Several data representations, based on all the attributed formulas, can eventually be used for comparison to reference samples.

Fig. 10 displays the mass spectrum of the sample collected in ESI positive mode between 150 and 800 Da. The intensity profile, with a maximum intensity around 320 Da, shares similarities with those of N-rich tholins acquired in similar analytical conditions (Vuitton et al., 2021; Moran et al., 2020; Maillard et al., 2018; Jovanovic et al., 2020). However, the intensity profile decreases more slowly, with less than one decade of intensity between 320 and 800 Da. Repetitive intensity patterns are observed in the spectrum, similarly to the abovementioned tholins. They are usually described as a signature of polymerization, the mass difference between two consecutive maxima being an averaged value of several monomers. Here, the value of 14.016 Da shows that the polymerization growth is dominated by the addition of CH_2 molecular groups. Similar observations can be achieved from the ESI negative mode mass spectrum.

A standardized process was used to assign a unique molecular formula to ions peaks over the entire mass range (m/z=150-800 Da) (Vuitton et al., 2021). A unique formula is first assigned to a peak at low mass, and peaks at heavier mass are then identified through the addition of CH_2 (alkylation) or other building groups (C, O, NH). Overall, the nature of the building blocks appear in a Mass defect-versus-Mass (MDvM) diagram, where the mass defect is the difference between the exact mass and the closest nominal mass (Fig. 11). The MDvM plot allows direct visual recognition of point alignments representing monomers that separate repetitive molecular groups. Trends due to CH_2, O and H_2 groups are displayed in Figure 11.

The full assignment led to 6596 exact stoichiometric formulae, which represents several tens or hundred thousands of individual compounds due to the large number of isomers for each mass. The unsaturation was estimated through the double-bound equivalents (DBE), defined as the number of rings plus the number of double and triple bonds in a neutral molecule. It was calculated from each stoichiometric formula $C_cH_hO_oN_n$ as:

$$DBE(C_cH_hO_oN_n) = c - \frac{h}{2} + \frac{n}{2} + 1 \quad (5)$$

Even if oxygen is known to create double bounds like in ketones or carboxylic acids, it does not control unsaturation (as the number of double bonds and rings, and a triple bond corresponding to 2 double bonds). As our sample is essentially made of C, H and O atoms, unsaturation is only achieved by carbon and hydrogen. Figure 12 displays two representations of stoichiometric diversity of the residue. On the left, O/C value is plotted against mass for varying number of oxygen atoms. For a given oxygen value, data points appear as a hyperbolic distribution, consistent with other sample analyses (Maillard et al., 2018; Moran et al., 2020). This representation is a way to assess the attribution quality, as any misattribution will appear on the wrong hyperbolic line. This diagram also shows that the radiolytic process populates all oxygen levels. Hence, we are not only observing O_1-bearing molecules that could refer to alcohol, phenol, or epoxy chemical functions, or O_2-bearing molecules that could refer to carboxylic acids, but a broad diversity of molecular structures that contain several oxygenated groups. This points to the complexity of the compounds and the lack of selectivity of the radiolytic chemical process. Figure 12 also reports the DBE value plotted against mass peak. As expected, the DBE values are not very high, as they are controlled only by carbon and hydrogen. In the case of N-rich tholins, the DBE distributions show values up to 40 due to the ability of nitrogen to promote unsaturation (Maillard et al., 2018). At a given number of oxygens, almost all DBE values are observed, indicating that the polymerisation process responsible for the unsaturation is weakly or not sensitive to the oxygen functionality. Note however that, due to the analytical technique, especially using the electrospray source as ionisation method, we are only sensitive to polar molecules. This means that this study does not investigate pure hydrocarbon diversity, i.e. when the number of oxygen is equal to zero.

Finally, the elemental ratio of the polar fraction of the residue were calculated from both ESI positive and negative modes by using the stoichiometric composition of mass peaks ponderated by peak intensities. We found H/C=1.50 ± 0.08 and O/C=0.4 ± 0.02. These estimates must be considered with care, because the ionisation yield is controlled by the molecular structure, which must promote protons exchange with the solvent.

4.2. CD_3OD - $^{58}Ni^{9+}$ at 33.1 MeV

The irradiation of CD_3OD with $^{58}Ni^{9+}$ ions resulted in the production of similar simple by-products as CO, CO_2 and D_2CO and HDCO, detected by FTIR spectroscopy and MS/QMS (Fig. 13). CD_4 could not be detected because the position of its bands was coincident with broad features of methanol. Interestingly, we observed the formation of D_2O molecules, demonstrating that water is also a by-product of methanol irradiation. This confirms that the water signatures in the infrared spectra collected during the TPD sequence are not controlled by contamination from the residual vacuum in the chamber.

We have estimated the band strengths of several vibration modes of pure CD_3OD from experiments run at IPAG at 20 K, using a He-Ne laser for determining the film thickness (Appendix A). We then determined the radiolytic destruction cross-section of deuterated methanol, by fitting the first derivative of the column density with the following relationship:

$$-\frac{dN}{dF} = \sigma_d N + Y \tag{6}$$

The fit led to σ_d=(1.5 ± 0.6) x 10^{-13} $cm^2.ion^{-1}$. We have compared this value to the data of de Barros et al. (2011) and Dartois et al. (2019) (Fig. 14). The reanalysis of earlier data by Dartois et al. (2019) led to a destruction cross-section of methanol of (4.14 ± 2.0) x $10^{-17} S_e^{1.11\pm0.11}$. However, one cross-section from de Barros et al. (2011) was not reported correctly, and the error estimated by these authors (± 5 %) was clearly underestimated. We run again this fit with more realistic errors (± 25 %) and got σ_d = (5.5 ± 3.0) x $10^{-17} S_e^{1.06\pm0.08}$. The destruction cross-section derived for CD_3OD in this study lies at the edge of the 95% confidence area, and is consistent with CH_3OH data. As it is based on the destruction of the C-O bond, the effect of D atoms appears weak or negligible.

4.3. CH_3OH - $^{18}O^{6+}$ at 105 keV

The conditions of CH_3OH ice irradiation with low energy $^{18}O^{6+}$ ions are different from the two previous experiments run with swift heavy ions. The penetration depth is lower than the thickness of the film, ions eventually implant and the deposited dose varies upon depth. Moreover, there is a significant contribution of elastic interactions (See S_n versus S_e in Tab. 3). Even though those conditions are different, we observe qualitatively a similar evolution of methanol ice: formation of CO, CO_2, H_2CO and CH_4 as simple byproducts, and similar bands assigned to organics (C=O, C=C, CH_x groups) (Fig. 13). After the sublimation of ices, a residue was recovered at room temperature, which

shares similarities with those recovered in experiment E_1. In details, we observe slight differences in the shape of the $B_{C=O,C}$ band that ranges from 1500 to 1800 cm^{-1}. This experiment shows that, at least qualitatively, the final organic material does not depend significantly on the ion energy over 4 orders of magnitudes. The same mechanisms seem to be at play, which is consistent with observations on simple polymers that do not contain aromatic species (Faure et al., 2021). Interestingly, the presence of elastic interactions does not modify the main composition of the organics.

5. Discussion

5.1. Organic by-products: chemical routes and composition

Our experiments show that complex organics are formed from pure methanol ice for electronic doses consistent with those at Arrokoth surface, down to 1 m deep. These complex organics are a mixture of molecules spanning a broad range of weight, from a few to several hundred C atoms. The most refractory fraction recovered at room temperature is essentially soluble in polar solvents. The similarity of the infrared features in the region 1800-1200 cm^{-1}across 40-300 K points to a continuum, i.e. species bearing similar chemical groups as OH, CH, CH_2, CH_3, olefinic C=C and, in weaker abundance, C≡C. The molecular complexity is high, with 6596 molecular formulas and several hundred of thousands of molecules. The formation mechanisms includes bond breaking, radical recombination and sputtering of atoms and molecules in the gas phase. The large H_2 signal in the QMS spectra reveals a large dehydrogenation, turning the initial H/C ratio from 4 to 1.5 in the refractory residue collected at room temperature. The formation of olefinic and acetylinic bonds results from the recombination of adjacent carbon radicals (Balanzat et al., 1995; Steckenreiter et al., 1999; Severin et al., 2010). Interestingly, the chemical evolution of methanol ice shares similarities with the irradiation of simple oxygenated polymers, e.g. poly-ethylene-glycol (PEG) (Faure et al., 2021). The infrared spectra of irradiated PEG display similar features in the range 1800-1200 cm^{-1}, CO and CO_2 as simple by-product, and overall the spectral evolution looks similar between the two materials. Noteworthy is the abundance of OH groups, very weak or negligible in irradiated PEG compared to irradiated methanol. A large fraction of the initial hydroxyl groups in methanol are then preserved during the irradiation of methanol ice. The profile of the band $B^s_{CH_x}$ points to a significant proportion of methylene versus methyl groups (n_{CH_2}/n_{CH_3} around 1 at 210 K and 0.83 at 300 K), which supports short alkyl chains and significant cross-linking.

Irradiated methanol also shares similarities with organic solids produced from cold plasma vapor deposition (e.g. Phan et al. (2021)). The HCO tholin from that study is made of C=O, C=C, CHx and OH groups, and accordingly the infrared spectra are fairly similar. The relative abundances of these chemical groups are, however, not strictly similar to those of the methanol residue, which result from the initial composition of the gas mixture injected in the plasma reactor and/or the physical conditions in the plasma. This points to similarities between the physical processes at play in a cold plasma experiment and in an irradiated solid. Structural and chemical effects triggered by swift heavy ions in solids can be accounted for by the thermal spike model (Toulemonde et al., 1993). In this model, incoming ions interact with electrons, which are locally released and leave ionized tracks (diameter ∼ 1 nm). The interactions of these electrons with atoms generate electronic cascades and a plasma with high-temperature electrons, which eventually transfer kinetic energy to the atomic lattice and trigger a temperature surge of several thousands of degrees for atoms in the lattice. This temperature surge is responsible of sputtering in the vicinity of the sample surface. The whole sequence of these processes is shorter than 1 ns, i.e. it is an ultra-fast pyrolysis that is very difficult to simulate in the laboratory, even by means of femto-second laser (Toulemonde et al., 1993). The thermal degradation of organic material through fast pyrolysis (∼ 1 s) leads to aromatic-rich residues (Cui et al., 2016), which are very different from irradiated methanol or oxygenated polymer (Faure et al., 2021). The similarities between irradiated and cold plasma materials support the view that temperature is not the main physical parameter that controls chemistry. Estimates of the atomic peak temperature by the thermal spike model are usually around 2000-3000 K, but they decrease very rapidly across the track. Furthermore, the very short heating duration probably largely inhibits the aromatization process. Finally, bond breaking and recombination during electronic cascades would dominate irradiation chemistry, which are the conditions that prevail in cold plasmas. Altogether, this suggests that cold plasma materials formed in the laboratory (tholins) should be considered as fair analogs of irradiated solid materials.

The absorption properties of the organic material are controlled by conjugated olefinic groups. They are responsible for $\pi \rightarrow \pi^*$ electronic transitions that control absorption at short wavelength in the visible, thereby providing a reddish color. The abundance of conjugated bonds could not be determined, due to the spectral congestion of the $B_{C=O,C}$ band. The DBE provided by HRMS analysis provides insights into saturation, but includes ring with no unsaturated bonds.

In addition, only conjugated olefinic bonds lead to visible absorption. In this respect, linking the chemical composition to the absorption properties is not suitable with our set of data.

5.2. Relevance to planetary conditions

The irradiation experiment $E_1$was run with a $^{136}Xe^{19+}$ ion, while calculations show that H and He are the main contributor of the dose deposited in Arrokoth's surface. According to de Barros et al. (2011), the destruction cross section of methanol ice is written as AS_e^n, with A is a pre-exponential factor and n ranges between 1 and 1.5. Our reevaluation of this cross section leads to an exponent n between 0.98 and 1.14. Because $n \neq 1$, $^{136}Xe^{19+}$ achieve faster methanol ice destruction than H at the same equivalent dose, and we overestimate the rate of chemical evolution in planetary conditions. Taking electronic stopping powers at 0.55 MeV/u, the ratio of $[S_e^n(136Xe)/S_e^n(H)]/[S_e(136Xe)/S_e(H)]$ is equal to 2.1, 4 and 525 for $n = 1.14$, 1.25 and 1.5, respectively. These values span a broad range and show that the exponent is a critical parameter. But with an upper value of 1.14, the impact is quite limited. H irradiation of methanol ice and methanol:water mixtures by Moore et al. (1996) were achieved with a dose of 34 eV/molecule (against $\sim$ 36 eV/molecule in our experiment). The organic residue from that study measured at 220 K (spectrum (a) in Fig. 4) displays the same bands B_{OH}, $B^s_{CH_x}$, $B_{C=O,C}$ and $B^b_{CH_x}$ displayed by our sample at the same temperature, pointing to similarities in the chemical routes. The shape of $B_{C=O,C}$ appears however more similar to that in our low energy experiments E3 and E4. We also note the presence of the 1041 cm^{-1}band, due to the C-O bond, which may be more difficult to break with protons. In the case of He, the second contributor to the electronic dose in Arrokoth's subsurface, the ratio $[S_e^n(136Xe)/S_e^n(He)]/[S_e(136Xe)/S_e(He)]$ is equal to 1.7, 2.5 and 6.4 for $n = 1.14$, 2.5 and 6.5, respectively. In this respect, the $^{136}Xe^{19+}$ ion fits better the contribution of He, but further experiments are necessary to get an appraisal of chemical similarities and differences of the final by-product. For C, N, O, Mg, Si and Fe, which probe the depth 1-1000 mm, we infer that the $^{136}Xe^{19+}$ ion experiments are more representative of the planetary conditions. Another point to address is the presence of a thermally-activated chemistry during TPD. Molecular diffusion, radical recombination and other chemical reactions happen in the sample during warming up. However, these chemical reactions do not lead to a major evolution of the organics. The characteristic features $B_{C=O,C}$ and $B^b_{CH_x}$ are present from 10 K to room temperature, showing that aliphatic, olefinic and carbonyl groups are the main chemical groups composing the organics.

At the surface of Arrokoth, CH_3OH may be, or may have been mixed with other molecules, e.g. H_2O. A concentration effect can then be expected. Moore et al. (1996) have investigated mixtures with the H_2O:CH_3OH =1:0.6 composition, and mixtures dominated by methanol. For these concentrations, any methanol molecules is surrounded by other methanol molecules, therefore polymerization and chemical growth are expected. Their spectra collected at 220 K show similar organic features. At 10% concentration, calculations of Behringer (1958) run for crystalline cubic solids, show that 30-50% of molecules should be present as monomer, 20% as dimers, and the rest as multimers. At 1% concentration, the abundance of monomers is around 90%, which decreases the abundance of chromophores by one order of magnitude. This conclusion holds if the surrounding matrix is devoid of C atoms, not in the case of other species like H_2CO, CO_2 or CH_4, which would react with methanol.

Last, the actual conditions in the subsurface may lead to hypervolatile (H_2 or CO) trapping at some depth, either in the water lattice or as bubble. In thin films experiments, volatiles can escape more easily. These trapped molecules would react further, changing the chemistry, for instance through mitigating dehydrogenation. In addition, our calculations do not include secondary reactions at high energy that generate gamma radiation, and contribute to the total dose. To get an appraisal of this contribution, we have run simulations on a crystalline water ice surface in the same physical conditions as Loeffler et al. (2020), who considered these secondary reactions using the GEANT4 software. Comparing our results with theirs shows that our calculation underestimates the dose by a factor ranging 2-7 in the first meter of the subsurface.

5.3. A reddening scenario for Arrokoth's surface

A reddening scenario of Arrokoth's surface is taking place based on the above results (Fig. 15). Our calculations show that sputtering is essentially controlled by SW and SEPs (Tab. 2). The erosion of organics (formed by radiolysis) is the lowest over 4.55 Gyr, compared to ices. Above $\sim$ 10 mm, the effect of sputtering disappears. Because materials display very different responses to sputtering, a chemical fractionation is expected in the first millimeters of the surface, which corresponds to the depth probed by the MVIC and LEISA spectrometers. Hyper-volatiles (e.g. CO) and volatiles (CO_2, CH_4, H_2CO) will get less and less abundant, and even water ice may become a weak component with respect to organic species. We may infer that eventually sputtering could generate an organic crust, covering a more icy material.

Accordingly, the detection of buried icy species would be difficult. However, the detection of methanol at the surface of Arrokoth along with the non detection of water ice raises questions, as the sputtering yield of methanol is higher than that of water ice. In the case of Centaur Pholus (Cruikshank et al., 1998), TNO (55638), TNO 2002 VE_{95} and TNO (120348) 2004 TY364, water ice could be present as mixed with methanol (Merlin et al., 2012).

The contribution of SW to ice radiolysis is weak. The nuclear dose lies above 10 eV.atom^{-1} in the first 30 nm, and organics formed from ice radiolysis should be transformed into dark amorphous carbons (Faure et al., 2021). However, its presence at the very top of the surface during 4.55 Gyr is unlikely, due to burying and mixing processes triggered by regolith gardening. GCRs leave high electronic doses in the range 50-200 eV/atom in the first 100 μm. Experiments on polymers show that their evolution upon increasing doses includes two stages (Calcagno et al., 1992). The first consists in scission, cross-linking and bond creation within chains. The respective contribution of these processes depend on the nature of the polymer, i.e. linear or reticulated structure, molecular weigh of chains, composition of monomers. PTFE (Polytetrafluoroethylene) is for instance very sensitive to chain scission and show a significant sputtering yield, while PE (polyethylene) or PS (polystyrene) are very resistant and promote instead cross-linking. PMMA (Poly(methyl methacrylate)) and PEG (polyethylene glycol) that contain tetrahedral carbons are somewhere in-between (Calcagno et al., 1992; Balanzat et al., 1995; Faure et al., 2021). In a second stage, further irradiation promotes extensive dehydrogenation and sp^2 carbon, forming material that share similarities with hydrogenated amorphous carbons. According to (Calcagno et al., 1992), the end of the first stage is a material whose composition and structure are irrespective of the starting polymer, and whose subsequent evolution is essentially controlled by the dose. However, the nature of the dose (elastic versus electronic) is a key factor and several precursors evolve towards amorphous carbon even at low electronic dose, if the elastic dose is higher than 10^{+10}_{-7}eV.atom^{-1}. In addition, the presence of radio-resistant aromatic species in the polymer tend to form polyaromatic by-products after extensive electronic irradiation (Costantini et al., 2002, 2005). In the case of methanol ice, a cross-linked organic macromolecular compound is achieved at electronic doses in the range 5-20 eV.atom^{-1}. Following Calcagno et al. (1992), we expect a progressive H loss and sp^2/sp^3 increase, and finally a range of hydrogenated amorphous carbons with varying Tauc gap and optical absorptions. Experiments run until a 200 eV.atom^{-1} electronic dose are here necessary to quantify the absorption properties of this familly of hydrogenated amorphous carbons.

In contrast to Solar ions, Galactic cosmic-rays control methanol ice radiolysis as deep as several meters in Arrokoth's subsurface. The electronic dose is significant in the first meter ($>$ 1 eV/atom), and we expect a signficant abundance of reddish organics. The main contributing ions to radiolysis are H and He. Other ions provide a dose lower by $\sim$ one order of magnitude and only within the first meter. The destruction yield calculated with a revised destruction cross-section from de Barros et al. (2011) also meets this conclusion (Fig. 3), as we obtain, for protons at 44 au, a destruction yield $>$ 10%. The deep penetration of H and He ions mitigate the effect of regolithic turn-over that tends to lower the actual irradiation time.

However, other processes control the surface evolution of Kuiper Belt objects (Stern, 2003). The surface of Arrokoth has been exposed to interplanetary dust particles (IDPs) and interstellar grains (ISG) fluxes, leading to surface ablation and regolith gardening (Poppe, 2015, 2016; Szalay et al., 2018). Poppe (2015) has estimated the mass ejecta rate at the Pluto system using the IDP and ISG fluxes derived from dust models and the crater yield determined from laboratory simulations (Koschny & Grun, 2001). If we take the average value of these estimates that vary during the Pluto year, we obtain an ablation rate of $\sim$ 30 μm.Myr^{-1} for water ice, i.e. $\sim$ 14 cm. The analysis of the data collected by the Student Dust Counter aboard New Horizons spacecraft led to higher estimates between 30 and 300 μm.Myr^{-1} (Bernardoni et al., 2022). However, these values are likely overestimated, in particular because the experimental conditions of Koschny & Grun (2001) do not strictly fit planetary conditions (ice temperature was 250 K against 40 K, projectiles were glass particles against fragile chondritic porous assemblages). In addition, organic materials are more resistant to hypervelocity impact. Shock experiments in the laboratory show that Titan's tholins are carbonized and transformed into a polyaromatic residue, with a moderate mass loss (Quirico et al., 2019). Last, impacting particles or their fragments may remain stuck at the surface, thereby contributing to the spectral properties of Arrokoth's surface.

Other processes that possibly mitigate a radiolytic origin of red organics are catastrophic surface ablation events triggered by (i) crossing Giant Molecular Clouds, (ii) passing stars or supernovae heating and (iii) collisions (Stern, 2003). Crossing giant molecular clouds would enhance the flux of ISGs at the surface, thereby increasing the ablation rate of ice. It is however difficult to constrain the frequency and intensity dust surges that happened in the past. Heating by passing stars or supernovae may have been significant in the Kuiper belt at the early stages of Solar System formation, but no later than 2 Myr, which means a lack of thermal destabilisation during almost 4.55 Gyr (Pfalzner,

2013). Collisions between KBOs are in contrast a frequent process that shaped the present size distribution of KBOs (Abedin et al., 2021). Low-sized KBOs (< 10-20 km) would be collisionally evolved, and most collisions would have likely happened within the main classical belt at low collisional speed (< km.s^{-1}). Recent fragmentation would have delivered fragments with fresh and weakly irradiated surface. It is however unclear whether Arrokoth has experienced a recent collision. In the case of small impactors, the physics of collision of icy porous bodies, and consequently effects on optical and chemical properties of an impacted surface remain poorly known (Leinhardt et al., 2007).

Finally, the formation of reddish organic materials is supported by calculations and experimental simulations. The deep penetration of GCRs generate organics deep enough to escape ablation processes such as sputtering and dust bombardment. This provides evidence that Arrokoth's red surface has not a primordial origin, but is a direct consequence of space weathering. Future studies should focus on the optical properties of the radiolytic organic byproducts, as there is yet no direct evidence that these materials fit MVIC and LEISA observations. The determination of the absorption properties of irradiated methanol is tricky due to the contribution of scattering, but a way to circumvent this problem could be to produce analogs in cold plasma reactors. The room-temperature residue could also be tentatively characterized by combined FTIR and VUV measurements after dissolution in different solvents, suitable with both spectral ranges.

6. Conclusions

The main conclusions of this study are the following:

1. SW control the sputtering rate of Arrokoth's surface.This erosion thickness is estimated at ~ 240 μm in the case of water ice, and at a few μm for organic materials. Sputtering tends to favor the formation of a pure organic crust at the surface.
2. SEPs generate a nuclear dose greater than the critical dose 10^{+10}_{-7} eV/atom and a significant electronic dose (until 200 eV.atom^{-1}) in the first tens of nm of the surface. A range of hydrogenated amorphous carbons may form there, with varying optical properties depending on the dose.
3. Extrapolating the differential flux of SW and SEPs measured at 1 au at high heliocentric distance leads to an overestimate of sputtering yields by one order of magnitude. Dedicated models need to be used.
4. GCRs dominate radiolysis in the first meter of the subsurface, and generate macromolecular reddish organic compounds. This deep chemistry mitigates the effect of regolithic turnover that tends to limit the actual irradiation time of grains.
5. Macromolecular organics formed from pure methanol ice are a complex mixture of tens or hundreds thousands of compounds. The main functional groups are CH_x, carbonyl C=O, olefinic C=C and -OH. Optical absorption through $\pi \rightarrow \pi^*$ is controlled by conjugated C=C bonds.
6. Tholins, which are polymeric amorphous macromolecular solids formed in cold plasma reactors, appear as fair analogues of irradiation by-products, and could be helpful to determine their optical properties.
7. According to these numerical and experimental results, the formation of reddish organics at Arrokoth's surface from methanol-rich ices by GCRs radiolysis (and to a lesser extent SEPs) appears plausible. This holds in the lack of ancient events (interplanetary and interstellar dust impacts, collisions) that would have ablated several meters of the surface.

7. Acknowledgements

This work has been funded by the ANR project CLASSY (Grant ANR-17- CE31-0004-02) of the French Agence Nationale de la Recherche and by the Centre National dÓEtudes Spatiales (CNES-France). We are very grateful to the Grand Accelérateur National d'Ions Lourds (GANIL - Caen) for time allocated on the IRRSUD and ARIBE beamlines in 2019, 2020 and 2021. Belén Maté (IEM-CSIC, Spain) is warmly thanked for discussion about determination of methanol ice density. We are very grateful to the comments and suggestions of two anonymous reviewers which improved the manuscript.

Table 4
Band strengths of CD_3OD.

Vibration mode	Band strength (cm/molec)	Integration range (cm^{-1})
γ CD_3	$4.0 \pm 0.2 \times 10^{-19}$	889-913
δ CD_3 as	$1.5 \pm 0.1 \times 10^{-18}$	1050-1075
δ CD_3 s	$7.2 \pm 0.4 \times 10^{-18}$	1079-1166
ν CD_3 as	$7.5 \pm 0.4 \times 10^{-18}$	2196-2263
ν CD_3 s	$4.4 \pm 0.3 \times 10^{-18}$	2054-2104
ν CO as	$8.3 \pm 0.5 \times 10^{-18}$	941-1005

as=antisymmetric. s=symmetric.

A. Measurements of the band strengths of CD_3OD ice

Experiments were run at IPAG with a Bruker Vertex70v spectrometer, equipped with a DTGS detector, a KBr beamsplitter and a Globar source. The spectral resolution was 1 cm^{-1}. Thin films were produced in a chamber maintained under secondary vacuum (typically, 5 x 10^{-7} mbar), by condensation onto a KBr window at 24 K. The film growth was monitored with a He-Ne laser at an incidence angle of 45 °. Interference fringes were used to determine the sample thickness, using the refractive index of liquid methanol n=1.33 (Bouilloud et al., 2015). The density of solid CD_3OD has not been determined experimentally. We have used the value 0.796 $g.cm^{-3}$, calculated by scaling the density of amorphous CH_3OH (0.71 $g.cm^{-3}$) with the density of liquid CH_3OH and CD_3OD. The band strengths of 6 vibration modes were then determined (Tab. 4).

B. Measurements of gaseous products by QMS

Gas by-products produced during irradiation and the Thermally Programmed Desorption (TPD) sequence were analyzed by means of a MKS Microvision 2 quadrupole mass-spectrometer (QMS). Masses from 1 to 100 were scanned continuously during the experiment (one full scan ~ 7s). The main volatile by-products were targeted (i.e. CH_3OH, H_2CO, CO, CO_2, CH_4, H_2 and H). No signal was detected above m/z=45, in particular organic species released after 210 K were not detected, while the corresponding IR spectra showed their disappearance from the solid sample. Fig. 16 displays the mass spectrum of pure methanol (during injection) and one spectrum collected during the TPD sequence. We clearly observe an intense peak at m/z=2, due to H2, which points to dehydrogenation. Excesses over the methanol peak at m/z=28, 29 and 31 essentially report the production of CO and H_2CO. m/z=18 points to the presence of H_2O, while m/z at 13, 14 and 15 point to the presence of CH_4. Fig. 17 reports the evolution of the intensity of the peak at m/z=2, 18, 28 and 32. During irradiation, H_2 and CO are the main by-products, while CO_2 was hardly detected at m/z=44. During TPD (Fig. 18), H_2 is essentially expelled at low temperature (<40 K). CO is essentially sublimated before 50 K, but sublimation continues until 120 K. At low temperature, H_2CO and O_2 (contamination from vacuum and produced from H_2O radiolysis) are expelled around 30 K. Methanol is sublimated between 130 and 155 K, and water has fully sublimated at 210 K. Note that this QMS monitoring is at best semi-quantitative: the data were not corrected from the electron-impact ionization cross-sections of the molecules, and we did not collect at the time of the experiment the fragmentation pattern of the by-products. In the case of methanol, the fragmentation pattern measured in our experiment and that provided by the NIST database were significantly different.

References

Abedin, A. Y., Kavelaars, J. J., Greenstreet, S., Petit, J.-M., Gladman, B., Lawler, S., Bannister, M., Alexandersen, M., Chen, Y.-T., Gwyn, S., & Volk, K. (2021). OSSOS. XXI. Collision Probabilities in the Edgeworth–Kuiper Belt. *AJ*, *161*, 195. URL: https://iopscience.iop.org/article/10.3847/1538-3881/abe418. doi:10.3847/1538-3881/abe418.

Adhikari, L., Zank, G. P., Bruno, R., Telloni, D., Hunana, P., Dosch, A., Marino, R., & Hu, Q. (2015). The transport of low-frequency turbulence in astrophysical flows. II. Solutions for the super-alfvenic solar wind. *ApJ*, *805*, 63. URL: https://iopscience.iop.org/article/10.1088/0004-637X/805/1/63. doi:10.1088/0004-637X/805/1/63.

Assmann, W., Davies, J., Dollinger, G., Forster, J., Huber, H., Reichelt, T., & Siegele, R. (1996). ERDA with very heavy ion beams. *Nuclear Instruments and Methods in Physics Research Section B: Beam Interactions with Materials and Atoms*, *118*, 242–250. URL: https://linkinghub.elsevier.com/retrieve/pii/0168583X95011838. doi:10.1016/0168-583X(95)01183-8.

Auge, B., Been, T., Boduch, P., Chabot, M., Dartois, E., Madi, T., Ramillon, J. M., Ropars, F., Rothard, H., & Voivenel, P. (2018). IGLIAS: A new experimental set-up for low temperature irradiation studies at large irradiation facilities. *Review of Scientific Instruments*, *89*, 075105. URL: http://aip.scitation.org/doi/10.1063/1.5028056. doi:10.1063/1.5028056.

Auge, B., Dartois, E., Duprat, J., Engrand, C., Slodzian, G., Wu, T. D., Guerquin-Kern, J. L., Vermesse, H., Agnihotri, A. N., Boduch, P., & Rothard, H. (2019). Hydrogen isotopic anomalies in extraterrestrial organic matter: role of cosmic ray irradiation and implications for UCAMMs. *A&A*, *627*, A122. URL: https://www.aanda.org/10.1051/0004-6361/201935143. doi:10.1051/0004-6361/201935143.

Auge, B., Dartois, E., Engrand, C., Duprat, J., Godard, M., Delauche, L., Bardin, N., Mejia, C., Martinez, R., Muniz, G., Domaracka, A., Boduch, P., & Rothard, H. (2016). Irradiation of nitrogen-rich ices by swift heavy ions: Clues for the formation of ultracarbonaceous micrometeorites. *A&A*, *592*, A99. URL: http://www.aanda.org/10.1051/0004-6361/201527650. doi:10.1051/0004-6361/201527650.

Balaji, V., David, D. E., Tian, R., Michl, J., & Urbassek, H. M. (1995). Nuclear sputtering of condensed diatomic gases. *J. Phys. Chem.*, *99*, 15565–15572. URL: https://pubs.acs.org/doi/10.1021/j100042a035. doi:10.1021/j100042a035.

Balanzat, E., Betz, N., & Bouffard, S. (1995). Swift heavy ion modification of polymers. *Nuclear Instruments and Methods in Physics Research Section B: Beam Interactions with Materials and Atoms*, *105*, 46–54.

de Barros, A. L. F., Domaracka, A., Andrade, D. P. P., Boduch, P., Rothard, H., & da Silveira, E. F. (2011). Radiolysis of frozen methanol by heavy cosmic ray and energetic solar particle analogues: Radiolysis of frozen methanol by heavy cosmic ray and energetic solar particle analogues. *Monthly Notices of the Royal Astronomical Society*, *418*, 1363–1374. URL: https://academic.oup.com/mnras/article-lookup/doi/10.1111/j.1365-2966.2011.19587.x. doi:10.1111/j.1365-2966.2011.19587.x.

Barucci, M. A., Belskaya, I. N., Fulchignoni, M., & Birlan, M. (2005). Taxonomy of Centaurs and Trans-Neptunian Objects. *AJ*, *130*, 1291–1298. URL: https://iopscience.iop.org/article/10.1086/431957. doi:10.1086/431957.

Behringer, R. E. (1958). Number of Single, Double, and Triple Clusters in a System Containing Two Types of Atoms. *The Journal of Chemical Physics*, *29*, 537–539. URL: http://aip.scitation.org/doi/10.1063/1.1744537. doi:10.1063/1.1744537.

Behrisch, R., Prozesky, V., Huber, H., & Assmann, W. (1996). Hydrogen desorption induced by heavy-ions during surface layer analysis with ERDA. *Nuclear Instruments and Methods in Physics Research Section B: Beam Interactions with Materials and Atoms*, *118*, 262–267. URL: https://linkinghub.elsevier.com/retrieve/pii/0168583X95010947. doi:10.1016/0168-583X(95)01094-7.

Bernardoni, E., Horányi, M., Doner, A., Piquette, M., Szalay, J. R., Poppe, A. R., James, D., Hunziker, S., Sterken, V., Strub, P., Olkin, C., Singer, K. N., Spencer, J., Stern, A., & Weaver, H. (2022). Student Dust Counter Status Report: The First 50 au. *Planet. Sci. J.*, *3*, 69. URL: https://iopscience.iop.org/article/10.3847/PSJ/ac5ab7. doi:10.3847/PSJ/ac5ab7.

Bouilloud, M., Fray, N., Benilan, Y., Cottin, H., Gazeau, M.-C., & Jolly, A. (2015). Bibliographic review and new measurements of the infrared band strengths of pure molecules at 25 K: H2O, CO2, CO, CH4, NH3, CH3OH, HCOOH and H2CO. *Monthly Notices of the Royal Astronomical Society*, *451*, 2145–2160. URL: http://academic.oup.com/mnras/article/451/2/2145/986563/Bibliographic-review-and-new-measurements-of-the. doi:10.1093/mnras/stv1021.

Boutard, D., Scherzer, B. M. U., & Möller, W. (1989). Ion-induced depletion of hydrogen from a soft carbonized layer. *Journal of Applied Physics*, *65*, 3833–3837. URL: http://aip.scitation.org/doi/10.1063/1.343399. doi:10.1063/1.343399.

Brown, M. E. (2012). The Compositions of Kuiper Belt Objects. *Annu. Rev. Earth Planet. Sci.*, *40*, 467–494. URL: http://www.annualreviews.org/doi/10.1146/annurev-earth-042711-105352. doi:10.1146/annurev-earth-042711-105352.

Brown, W. L., Augustyniak, W. M., Marcantonio, K. J., Simmons, E. H., Boring, J. W., Johnson, R. E., & Reimann, C. T. (1984). Electronic sputtering of low temperature molecular solids. *Nuclear Instruments and Methods in Physics Research Section B: Beam Interactions with Materials and Atoms*, *1*, 307–314.

Brunetto, R., Barucci, M. A., Dotto, E., & Strazzulla, G. (2006). Ion irradiation of frozen methanol, methane, and benzene: Linking to the colors of centaurs and trans-neptunian objects. *The Astrophysical Journal*, *644*, 646.

Calcagno, L., Compagnini, G., & Foti, G. (1992). Structural modification of polymer films by ion irradiation. *Nuclear Instruments and Methods in Physics Research Section B: Beam Interactions with Materials and Atoms*, *65*, IN7–422. URL: https://linkinghub.elsevier.com/retrieve/pii/0168583X92950775. doi:10.1016/0168-583X(92)95077-5.

Chrisey, D. B., Brown, W. L., & Boring, J. W. (1990). Electronic excitation of condensed CO: Sputtering and chemical change. *Surf. Sci.*, *225*, 130–142.

Cooper, J. F., Christian, E. R., Richardson, J. D., & Wang, C. (2003). Proton Irradiation of Centaur, Kuiper Belt, and Oort Cloud Objects at Plasma to Cosmic Ray Energy. *Earth, Moon and Planets*, *92*, 261–277.

Costantini, J.-M., Couvreur, F., Salvetat, J.-P., & Bouffard, S. (2002). Micro-Raman study of the carbonization of polyimide induced by swift heavy ion irradiations. *Nuclear Instruments and Methods in Physics Research Section B: Beam Interactions with Materials and Atoms*, *194*, 132–140. URL: https://linkinghub.elsevier.com/retrieve/pii/S0168583X02006699. doi:10.1016/S0168-583X(02)00669-9.

Costantini, J.-M., Salvetat, J.-P., Couvreur, F., & Bouffard, S. (2005). Carbonization of polyimide by swift heavy ion irradiations: Effects of stopping power and velocity. *Nuclear Instruments and Methods in Physics Research Section B: Beam Interactions with Materials and Atoms*, *234*, 458–466. URL: https://linkinghub.elsevier.com/retrieve/pii/S0168583X05001631. doi:10.1016/j.nimb.2005.01.117.

Cruikshank, D., Roush, T., Bartholomew, M., Geballe, T., Pendleton, Y., White, S., Bell, J., Davies, J., Owen, T., de Bergh, C., Tholen, D., Bernstein, M., Brown, R., Tryka, K., & Dalle Ore, C. (1998). The Composition of Centaur 5145 Pholus. *Icarus*, *135*, 389–407. URL: https://linkinghub.elsevier.com/retrieve/pii/S0019103598959978. doi:10.1006/icar.1998.5997.

Cruikshank, D. P., Imanaka, H., & Dalle Ore, C. M. (2005). Tholins as coloring agents on outer Solar System bodies. *Advances in Space Research*, *36*, 178–183. URL: http://linkinghub.elsevier.com/retrieve/pii/S0273117705009373. doi:10.1016/j.asr.2005.07.026.

Cui, T., Fan, W., Dai, Z., Guo, Q., Yu, G., & Wang, F. (2016). Variation of the coal chemical structure and determination of the char molecular size at the early stage of rapid pyrolysis. *Applied Energy*, *179*, 650–659. URL: https://linkinghub.elsevier.com/retrieve/pii/S030626191630931X. doi:10.1016/j.apenergy.2016.06.143.

Cummings, A. C., Stone, E. C., Heikkila, B. C., Lal, N., Webber, W. R., Jóhannesson, G., Moskalenko, I. V., Orlando, E., & Porter, T. A. (2016). Galactic cosmic rays in the local interstellar medium: voyager observations and model results. *ApJ*, *831*, 18. URL: https://iopscience.

737 iop.org/article/10.3847/0004-637X/831/1/18. doi:10.3847/0004-637X/831/1/18.
738 Dartois, E., Augé, B., Boduch, P., Brunetto, R., Chabot, M., Domaracka, A., Ding, J. J., Kamalou, O., Lv, X. Y., Rothard, H., da Silveira, E. F., &
739 Thomas, J. C. (2015). Heavy ion irradiation of crystalline water ice: Cosmic ray amorphisation cross-section and sputtering yield. *Astronomy &*
740 *Astrophysics*, *576*, A125. URL: http://www.aanda.org/10.1051/0004-6361/201425415. doi:10.1051/0004-6361/201425415.
741 Dartois, E., Chabot, M., Id Barkach, T., Rothard, H., Augé, B., Agnihotri, A. N., Domaracka, A., & Boduch, P. (2019). Non-thermal desorption of
742 complex organic molecules: Efficient CH $_3$ OH and CH $_3$ COOCH $_3$ sputtering by cosmic rays. *A&A*, *627*, A55. URL: https://www.aanda.
743 org/10.1051/0004-6361/201834787. doi:10.1051/0004-6361/201834787.
744 Dartois, E., Engrand, C., Brunetto, R., Duprat, J., Pino, T., Quirico, E., Remusat, L., Bardin, N., Briani, G., Mostefaoui, S., Morinaud, G., Crane,
745 B., Szwec, N., Delauche, L., Jamme, F., Sandt, C., & Dumas, P. (2013). UltraCarbonaceous Antarctic micrometeorites, probing the Solar System
746 beyond the nitrogen snow-line. *Icarus*, *224*, 243–252. URL: http://linkinghub.elsevier.com/retrieve/pii/S0019103513001103.
747 doi:10.1016/j.icarus.2013.03.002.
748 Dartois, E., Geballe, T. R., Pino, T., Cao, A.-T., Jones, A., Deboffle, D., Guerrini, V., Bréchignac, P., & d'Hendecourt, L. (2007). IRAS 08572+3915:
749 constraining the aromatic versus aliphatic content of interstellar HACs. *A&A*, *463*, 635–640. URL: http://www.aanda.org/10.1051/
750 0004-6361:20066572. doi:10.1051/0004-6361:20066572.
751 Dollinger, G., Boulouednine, M., Bergmaier, A., Faestermann, T., & Frey, C. (1996). Limits in elastic recoil detection analysis with heavy
752 ions. *Nuclear Instruments and Methods in Physics Research Section B: Beam Interactions with Materials and Atoms*, *118*, 291–300. URL:
753 https://linkinghub.elsevier.com/retrieve/pii/0168583X95014691. doi:10.1016/0168-583X(95)01469-1.
754 Doressoundiram, A., Boehnhardt, H., Tegler, S., & Trujillo, C. (2008). Color Properties and Trends of the Transneptunian Objects. In *The Solar*
755 *System Beyond Neptune* (p. 91). (University of arizona press, tucson ed.).
756 Fama, M., Shi, J., & Baragiola, R. (2008). Sputtering of ice by low-energy ions. *Surface Science*, *602*, 156–161. URL: https://linkinghub.
757 elsevier.com/retrieve/pii/S0039602807009879. doi:10.1016/j.susc.2007.10.002.
758 Faure, M., Quirico, E., Faure, A., Boduch, P., Rothard, H., Balanzat, E., Baklouti, D., Brunetto, R., Bonal, L., Beck, P., & Schmitt, B. (2021). A
759 radiolytic origin of organic matter in primitive chondrites and trans-neptunian objects? New clues from ion irradiation experiments. *Icarus*, *364*,
760 114462. URL: https://linkinghub.elsevier.com/retrieve/pii/S0019103521001445. doi:10.1016/j.icarus.2021.114462.
761 Ferrari, A. C., & Robertson, J. (2000). Interpretation of Raman spectra of disordered and amorphous carbon. *Physical Review B*, *61*, 14095–14107.
762 URL: https://link.aps.org/doi/10.1103/PhysRevB.61.14095. doi:10.1103/PhysRevB.61.14095.
763 Ghosh, S., Avasthi, D., Som, T., Tripathi, A., Kabiraj, D., Ingale, A., Mishra, S., Ganesan, V., Zhang, S., & Hong, X. (2002). Structure
764 dependent electronic sputtering of a-C:H films by swift heavy ions. *Nuclear Instruments and Methods in Physics Research Section B: Beam*
765 *Interactions with Materials and Atoms*, *190*, 164–168. URL: https://linkinghub.elsevier.com/retrieve/pii/S0168583X01011971.
766 doi:10.1016/S0168-583X(01)01197-1.
767 Grundy, W. M., Bird, M. K., Britt, D. T., Cook, J. C., Cruikshank, D. P., Howett, C. J. A., Krijt, S., Linscott, I. R., Olkin, C. B., Parker, A. H.,
768 Protopapa, S., Ruaud, M., Umurhan, O. M., Young, L. A., Dalle Ore, C. M., Kavelaars, J. J., Keane, J. T., Pendleton, Y. J., Porter, S. B., Scipioni,
769 F., Spencer, J. R., Stern, S. A., Verbiscer, A. J., Weaver, H. A., Binzel, R. P., Buie, M. W., Buratti, B. J., Cheng, A., Earle, A. M., Elliott,
770 H. A., Gabasova, L., Gladstone, G. R., Hill, M. E., Horanyi, M., Jennings, D. E., Lunsford, A. W., McComas, D. J., McKinnon, W. B., McNutt,
771 R. L., Moore, J. M., Parker, J. W., Quirico, E., Reuter, D. C., Schenk, P. M., Schmitt, B., Showalter, M. R., Singer, K. N., Weigle, G. E., &
772 Zangari, A. M. (2020). Color, composition, and thermal environment of Kuiper Belt object (486958) Arrokoth. *Science*, *367*, eaay3705. URL:
773 https://www.science.org/doi/10.1126/science.aay3705. doi:10.1126/science.aay3705.
774 Hudson, R. L., Loeffler, M. J., Ferrante, R. F., Gerakines, P. A., & Coleman, F. M. (2020). Testing Densities and Refractive Indices of Extraterrestrial
775 Ice Components Using Molecular Structures—Organic Compounds and Molar Refractions. *ApJ*, *891*, 22. URL: https://iopscience.iop.
776 org/article/10.3847/1538-4357/ab6efa. doi:10.3847/1538-4357/ab6efa.
777 Jovanovic, L., Gautier, T., Vuitton, V., Wolters, C., Bourgalais, J., Buch, A., Orthous-Daunay, F.-R., Vettier, L., Flandinet, L., & Carrasco, N.
778 (2020). Chemical composition of Pluto aerosol analogues. *Icarus*, *346*, 113774. URL: https://linkinghub.elsevier.com/retrieve/
779 pii/S0019103520301615. doi:10.1016/j.icarus.2020.113774.
780 Khan, S. A., Tripathi, A., Toulemonde, M., Trautmann, C., & Assmann, W. (2013). Sputtering yield of amorphous 13C thin films under swift
781 heavy-ion irradiation. *Nuclear Instruments and Methods in Physics Research Section B: Beam Interactions with Materials and Atoms*, *314*,
782 34–38. URL: https://linkinghub.elsevier.com/retrieve/pii/S0168583X13006083. doi:10.1016/j.nimb.2013.05.044.
783 Koschny, D., & Grun, E. (2001). Impacts into Ice–Silicate Mixtures: Crater Morphologies, Volumes, Depth-to-Diameter Ratios, and Yield. *Icarus*,
784 *154*, 391–401. URL: https://linkinghub.elsevier.com/retrieve/pii/S0019103501967077. doi:10.1006/icar.2001.6707.
785 Kouchi, A. (1990). Evaporation of H2O-CO ice and its astrophysical implications. *J. Crys. Growth*, *99*, 1220–1226.
786 Lacerda, P., Fornasier, S., Lellouch, E., Kiss, C., Vilenius, E., Santos-Sanz, P., Rengel, M., Müller, T., Stansberry, J., Duffard, R., Delsanti, A., &
787 Guilbert-Lepoutre, A. (2014). THE ALBEDO-COLOR DIVERSITY OF TRANSNEPTUNIAN OBJECTS. *The Astrophysical Journal*, *793*, L2.
788 URL: http://stacks.iop.org/2041-8205/793/i=1/a=L2?key=crossref.e8ddc8dadca6f3d0974d8f23c34bd681. doi:10.1088/
789 2041-8205/793/1/L2.
790 Leinhardt, Z. M., Stewart, S. T., & Schultz, P. H. (2007). Physical effects of collisions in the Kuiper belt. URL: http://arxiv.org/abs/0705.
791 3943 number: arXiv:0705.3943 arXiv:0705.3943 [astro-ph].
792 Lin-Vien, D. (Ed.) (1991). *The Handbook of infrared and raman characteristic frequencies of organic molecules*. Boston: Academic Press.
793 Liu, M., Issautier, K., Meyer-Vernet, N., Moncuquet, M., Maksimovic, M., Halekas, J. S., Huang, J., Griton, L., Bale, S., Bonnell, J. W., Case,
794 A. W., Goetz, K., Harvey, P. R., Kasper, J. C., MacDowall, R. J., Malaspina, D. M., Pulupa, M., & Stevens, M. L. (2021). Solar wind energy
795 flux observations in the inner heliosphere: first results from Parker Solar Probe. *A&A*, *650*, A14. URL: https://www.aanda.org/10.1051/
796 0004-6361/202039615. doi:10.1051/0004-6361/202039615.
797 Loeffler, M. J., Tribbett, P. D., Cooper, J. F., & Sturner, S. J. (2020). A possible explanation for the presence of crystalline H2O-ice on Kuiper
798 Belt Objects. *Icarus*, *351*, 113943. URL: https://linkinghub.elsevier.com/retrieve/pii/S0019103520303171. doi:10.1016/j.
799 icarus.2020.113943.

Luna, R., Molpeceres, G., Ortigoso, J., Satorre, M. A., Domingo, M., & Maté, B. (2018). Densities, infrared band strengths, and optical constants of solid methanol. *A&A*, *617*, A116. URL: https://www.aanda.org/10.1051/0004-6361/201833463. doi:10.1051/0004-6361/201833463.

MacPhail, R. A., Strauss, H. L., Snyder, R., & Elliger, C. (1984). C-H Stretching Modes and the Structure of n-Alkyl Chains. 2. Long, All-Trans Chains. *J. Phys. Chem.*, *88*, 8.

Maillard, J., Carrasco, N., Schmitz-Afonso, I., Gautier, T., & Afonso, C. (2018). Comparison of soluble and insoluble organic matter in analogues of Titan's aerosols. *Earth and Planetary Science Letters*, *495*, 185–191. URL: https://linkinghub.elsevier.com/retrieve/pii/S0012821X18302851. doi:10.1016/j.epsl.2018.05.014.

Materese, C. K., Cruikshank, D. P., Sandford, S. A., Imanaka, H., & Nuevo, M. (2015). Ice chemistry on outer solar system bodies: electron radiolysis of N2, CH4, and CO-containing ices. *ApJ*, *812*, 150. URL: https://iopscience.iop.org/article/10.1088/0004-637X/812/2/150. doi:10.1088/0004-637X/812/2/150.

Merlin, F., Quirico, E., Barucci, M. A., & de Bergh, C. (2012). Methanol ice on the surface of minor bodies in the solar system. *Astronomy & Astrophysics*, *544*, A20. URL: http://www.aanda.org/10.1051/0004-6361/201219181. doi:10.1051/0004-6361/201219181.

Mewaldt, R. A., Cohen, C. M. S., Mason, G. M., Haggerty, D. K., & Desai, M. I. (2007). Long-Term Fluences of Solar Energetic Particles from H to Fe. *Space Sci Rev*, *130*, 323–328. URL: http://link.springer.com/10.1007/s11214-007-9200-8. doi:10.1007/s11214-007-9200-8.

Meyer, J.-P., Drury, L. O., & Ellison, D. C. (1998). A Cosmic-Ray Composition Controlled by Volatility and A/Q Ratio. SNR Shock Acceleration of Gas and Dust. In C. T. Russell, R. A. Mewaldt, & T. T. Von Rosenvinge (Eds.), *The Advanced Composition Explorer Mission* (pp. 179–201). Dordrecht: Springer Netherlands. URL: http://link.springer.com/10.1007/978-94-011-4762-0_9. doi:10.1007/978-94-011-4762-0_9.

Moore, M., Ferrante, R., & Nuth, J. (1996). Infrared spectra of proton irradiated ices containing methanol. *Planetary and Space Science*, *44*, 927–935. URL: https://linkinghub.elsevier.com/retrieve/pii/0032063395001204. doi:10.1016/0032-0633(95)00120-4.

Moran, S. E., Hörst, S. M., Vuitton, V., He, C., Lewis, N. K., Flandinet, L., Moses, J. I., North, N., Orthous-Daunay, F.-R., Sebree, J., Wolters, C., Kempton, E. M.-R., Marley, M. S., Morley, C. V., & Valenti, J. A. (2020). Chemistry of Temperate Super-Earth and Mini-Neptune Atmospheric Hazes from Laboratory Experiments. *Planet. Sci. J.*, *1*, 17. URL: https://iopscience.iop.org/article/10.3847/PSJ/ab8eae. doi:10.3847/PSJ/ab8eae.

Orthous-Daunay, F.-R., Thissen, R., & Vuitton, V. (2019). Measured mass to stoichoimetric formula through exhaustive search. *Proc. IAU*, *15*, 193–199. URL: https://www.cambridge.org/core/product/identifier/S1743921319008032/type/journal_article. doi:10.1017/S1743921319008032.

Painter, P. C., Snyder, R. W., Starsinic, M., Coleman, M. M., Kuehn, D. W., & Davis, A. (1981). Concerning the Application of FT-IR to the Study of Coal: A Critical Assessment of Band Assignments and the Application of Spectral Analysis Programs. *Applied Spectroscopy*, *35*, 475–485. URL: http://journals.sagepub.com/doi/10.1366/0003702814732256. doi:10.1366/0003702814732256.

Pawlak, F., Dufour, C., Laurent, A., Paumier, E., Perrière, J., Stoquert, J., & Toulemonde, M. (1999). Carbon sputtering of polymer-like amorphous carbon by swift heavy ions. *Nuclear Instruments and Methods in Physics Research Section B: Beam Interactions with Materials and Atoms*, *151*, 140–145. URL: https://linkinghub.elsevier.com/retrieve/pii/S0168583X99000890. doi:10.1016/S0168-583X(99)00089-0.

Perna, D., Barucci, M. A., Fornasier, S., DeMeo, F. E., Alvarez-Candal, A., Merlin, F., Dotto, E., Doressoundiram, A., & de Bergh, C. (2010). Colors and taxonomy of Centaurs and trans-Neptunian objects. *A&A*, *510*, A53. URL: http://www.aanda.org/10.1051/0004-6361/200913654. doi:10.1051/0004-6361/200913654.

Pfalzner, S. (2013). Early evolution of the birth cluster of the solar system. *A&A*, *549*, A82. URL: http://www.aanda.org/10.1051/0004-6361/201218792. doi:10.1051/0004-6361/201218792.

Phan, V. T., Quirico, E., Beck, P., Le Brech, Y., Jovanovic, L., Le Guillou, C., Bernard, S., Bonal, L., Carrasco, N., Gautier, T., & Raya, J. (2021). Infrared spectroscopy quantification of functional carbon groups in kerogens and coals: A calibration procedure. *Spectrochimica Acta Part A: Molecular and Biomolecular Spectroscopy*, *259*, 119853. URL: https://linkinghub.elsevier.com/retrieve/pii/S1386142521004297. doi:10.1016/j.saa.2021.119853.

Poppe, A. R. (2015). Interplanetary dust influx to the Pluto–Charon system. *Icarus*, *246*, 352–359. URL: https://linkinghub.elsevier.com/retrieve/pii/S001910351400027X. doi:10.1016/j.icarus.2013.12.029.

Poppe, A. R. (2016). An improved model for interplanetary dust fluxes in the outer Solar System. *Icarus*, *264*, 369–386. URL: https://linkinghub.elsevier.com/retrieve/pii/S0019103515004674. doi:10.1016/j.icarus.2015.10.001.

Quirico, E., Yabuta, H., Beck, P., Bonal, L., Bardyn, A., Nittler, L., Alexander, C. M. O., Carrasco, N., Latmos-Ipsl, I., & France, G. (2019). SUCCESS AND FAILURE OF SCHOCK RECOVERY EXPERIMENTS FOR SIMULATING SHORT DURATION PARENT BODY HEATING. *82nd Annual Meeting of The Meteoritical Society, held 7-12 July, 2019 in Sapporo, Japan. LPI Contribution No. 2157, 2019, id.6343*, *82*, 1.

Reuter, D. C., Stern, S. A., Scherrer, J., Jennings, D. E., Baer, J. W., Hanley, J., Hardaway, L., Lunsford, A., McMuldroch, S., Moore, J., Olkin, C., Parizek, R., Reitsma, H., Sabatke, D., Spencer, J., Stone, J., Throop, H., Van Cleve, J., Weigle, G. E., & Young, L. A. (2008). Ralph: A Visible/Infrared Imager for the New Horizons Pluto/Kuiper Belt Mission. *Space Sci Rev*, *140*, 129–154. URL: http://link.springer.com/10.1007/s11214-008-9375-7. doi:10.1007/s11214-008-9375-7.

Ribas, I., Guinan, E. F., Güdel, M., & Audard, M. (2005). Evolution of the solar activity over time and effects onn planetary atmospheres. I. High-energy irradiances (1-1700 A). *The Astrophysical Journal*, *622*, 680–694.

Schou, J., & Pedrys, R. (2001). Sputtering of carbon monoxide ice by hydrogen ions. *J. Geophys. Res.*, *106*, 33309–33314. URL: http://doi.wiley.com/10.1029/2000JE001281. doi:10.1029/2000JE001281.

Seperuelo Duarte, E., Domaracka, A., Boduch, P., Rothard, H., Dartois, E., & da Silveira, E. F. (2010). Laboratory simulation of heavy-ion cosmic-ray interaction with condensed CO. *Astronomy and Astrophysics*, *512*, A71. URL: http://www.aanda.org/10.1051/0004-6361/200912899. doi:10.1051/0004-6361/200912899.

Severin, D., Balanzat, E., Ensinger, W., & Trautmann, C. (2010). Outgassing and degradation of polyimide induced by swift heavy ion irradiation at cryogenic temperature. *Journal of Applied Physics*, *108*, 024901. URL: http://aip.scitation.org/doi/10.1063/1.3457846. doi:10.1063/1.3457846.

Shi, M., Grosjean, D., Schou, J., & Baragiola, R. (1995). Particle emission induced by ionization tracks in water ice. *Nuclear Instruments and Methods in Physics Research Section B: Beam Interactions with Materials and Atoms*, *96*, 524–529. URL: https://linkinghub.elsevier.com/retrieve/pii/0168583X95002499. doi:10.1016/0168-583X(95)00249-9.

Sigmund, P. (1969). Theory of Sputtering. I. Sputtering Yield of Amorphous and Polycrystalline Targets. *Phys. Rev.*, *184*, 383–416. URL: https://link.aps.org/doi/10.1103/PhysRev.184.383. doi:10.1103/PhysRev.184.383.

Stanishevsky, A. (2001). Patterning of diamond and amorphous carbon films using focused ion beams. *Thin Solid Films*, *398-399*, 560–565. URL: https://linkinghub.elsevier.com/retrieve/pii/S0040609001013189. doi:10.1016/S0040-6090(01)01318-9.

Steckenreiter, T., Balanzat, E., Fuess, H., & Trautmann, C. (1999). Pyrolytic effects induced by energetic ions in polymers. *Nuclear Instruments and Methods in Physics research B*, *151*, 161–168.

Stern, S. (2003). The evolution of comets in the Oort cloud and Kuiper belt. *Nature*, *424*, 639–642. URL: http://www.nature.com/articles/nature01725. doi:10.1038/nature01725.

Stern, S. A., Weaver, H. A., Spencer, J. R., Olkin, C. B., Gladstone, G. R., Grundy, W. M., Moore, J. M., Cruikshank, D. P., Elliott, H. A., McKinnon, W. B., Parker, J. W., Verbiscer, A. J., Young, L. A., Aguilar, D. A., Albers, J. M., Andert, T., Andrews, J. P., Bagenal, F., Banks, M. E., Bauer, B. A., Bauman, J. A., Bechtold, K. E., Beddingfield, C. B., Behrooz, N., Beisser, K. B., Benecchi, S. D., Bernardoni, E., Beyer, R. A., Bhaskaran, S., Bierson, C. J., Binzel, R. P., Birath, E. M., Bird, M. K., Boone, D. R., Bowman, A. F., Bray, V. J., Britt, D. T., Brown, L. E., Buckley, M. R., Buie, M. W., Buratti, B. J., Burke, L. M., Bushman, S. S., Carcich, B., Chaikin, A. L., Chavez, C. L., Cheng, A. F., Colwell, E. J., Conard, S. J., Conner, M. P., Conrad, C. A., Cook, J. C., Cooper, S. B., Custodio, O. S., Ore, C. M. D., Deboy, C. C., Dharmavaram, P., Dhingra, R. D., Dunn, G. F., Earle, A. M., Egan, A. F., Eisig, J., El-Maarry, M. R., Engelbrecht, C., Enke, B. L., Ercol, C. J., Fattig, E. D., Ferrell, C. L., Finley, T. J., Firer, J., Fischetti, J., Folkner, W. M., Fosbury, M. N., Fountain, G. H., Freeze, J. M., Gabasova, L., Glaze, L. S., Green, J. L., Griffith, G. A., Guo, Y., Hahn, M., Hals, D. W., Hamilton, D. P., Hamilton, S. A., Hanley, J. J., Harch, A., Harmon, K. A., Hart, H. M., Hayes, J., Hersman, C. B., Hill, M. E., Hill, T. A., Hofgartner, J. D., Holdridge, M. E., Horányi, M., Hosadurga, A., Howard, A. D., Howett, C. J. A., Jaskulek, S. E. et al. (2019). Initial results from the New Horizons exploration of 2014 MU69, a small Kuiper Belt object. *Science*, *364*, eaaw9771.

Stone, E. C., Cummings, A. C., McDonald, F. B., Heikkila, B. C., Lal, N., & Webber, W. R. (2013). Voyager 1 Observes Low-Energy Galactic Cosmic Rays in a Region Depleted of Heliospheric Ions. *Science*, *341*, 150–153. URL: https://www.science.org/doi/10.1126/science.1236408. doi:10.1126/science.1236408.

Szalay, J. R., Poppe, A. R., Agarwal, J., Britt, D., Belskaya, I., Horányi, M., Nakamura, T., Sachse, M., & Spahn, F. (2018). Dust Phenomena Relating to Airless Bodies. *Space Sci Rev*, *214*, 98. URL: http://link.springer.com/10.1007/s11214-018-0527-0. doi:10.1007/s11214-018-0527-0.

Torrie, B., Weng, S.-X., & Powell, B. (1989). Structure of the α-phase of solid methanol. *Molecular Physics*, *67*, 575–581. URL: http://www.tandfonline.com/doi/abs/10.1080/00268978900101291. doi:10.1080/00268978900101291.

Toulemonde, M., Paumier, E., & Dufour, C. (1993). Thermal spike model in the electronic stopping power regime. *Radiation Effects and Defects in Solids*, *126*, 201–206. URL: https://www.tandfonline.com/doi/full/10.1080/10420159308219709. doi:10.1080/10420159308219709.

Ullmann, J., Delan, A., & Schmidt, G. (1993). Ion etching behaviour and surface binding energies of hard diamond-like carbon and microwave chemical vapour deposition diamond films. *Diamond and Related Materials*, *2*, 266–271. URL: https://linkinghub.elsevier.com/retrieve/pii/092596359390066B. doi:10.1016/0925-9635(93)90066-B.

Urso, R. G., Baklouti, D., Djouadi, Z., Pinilla-Alonso, N., & Brunetto, R. (2020a). Near-infrared Methanol Bands Probe Energetic Processing of Icy Outer Solar System Objects. *ApJ*, *894*, L3. URL: https://iopscience.iop.org/article/10.3847/2041-8213/ab8ad9. doi:10.3847/2041-8213/ab8ad9.

Urso, R. G., Vuitton, V., Danger, G., Le Sergeant d'Hendecourt, L., Flandinet, L., Djouadi, Z., Mivumbi, O., Orthous-Daunay, F. R., Ruf, A., Vinogradoff, V., Wolters, C., & Brunetto, R. (2020b). Irradiation dose affects the composition of organic refractory materials in space: Results from laboratory analogues. *A&A*, *644*, A115. URL: https://www.aanda.org/10.1051/0004-6361/202039528. doi:10.1051/0004-6361/202039528.

Usoskin, I. G., Alanko-Huotari, K., Kovaltsov, G. A., & Mursula, K. (2005). Heliospheric modulation of cosmic rays: Monthly reconstruction for 1951–2004. *J. Geophys. Res.*, *110*, A12108. URL: http://doi.wiley.com/10.1029/2005JA011250. doi:10.1029/2005JA011250.

Vuitton, V., Moran, S. E., He, C., Wolters, C., Flandinet, L., Orthous-Daunay, F.-R., Moses, J. I., Valenti, J. A., Lewis, N. K., & Hörst, S. M. (2021). H_2SO_4 and Organosulfur Compounds in Laboratory Analogue Aerosols of Warm High-metallicity Exoplanet Atmospheres. *Planet. Sci. J.*, *2*, 2. URL: https://iopscience.iop.org/article/10.3847/PSJ/abc558. doi:10.3847/PSJ/abc558.

Vukovic, F., Leyssale, J.-M., Aurel, P., & Marks, N. A. (2018). Evolution of Threshold Displacement Energy in Irradiated Graphite. *Phys. Rev. Applied*, *10*, 064040. URL: https://link.aps.org/doi/10.1103/PhysRevApplied.10.064040. doi:10.1103/PhysRevApplied.10.064040.

Webber, W. R., & Yushak, S. M. (1983). A measurement of the energy spectra and relative abundance of the cosmic-ray H and He isotopes over a broad energy range. *ApJ*, *275*, 391. URL: http://adsabs.harvard.edu/doi/10.1086/161541. doi:10.1086/161541.

Wolters, C., Flandinet, L., He, C., Isa, J., Orthous-Daunay, F., Thissen, R., Horst, S., & Vuitton, V. (2020). Enhancing data acquisition for the analysis of complex organic matter in direct-infusion Orbitrap mass spectrometry using micro-scans. *Rapid Commun Mass Spectrom*, *34*. URL: https://onlinelibrary.wiley.com/doi/10.1002/rcm.8818. doi:10.1002/rcm.8818.

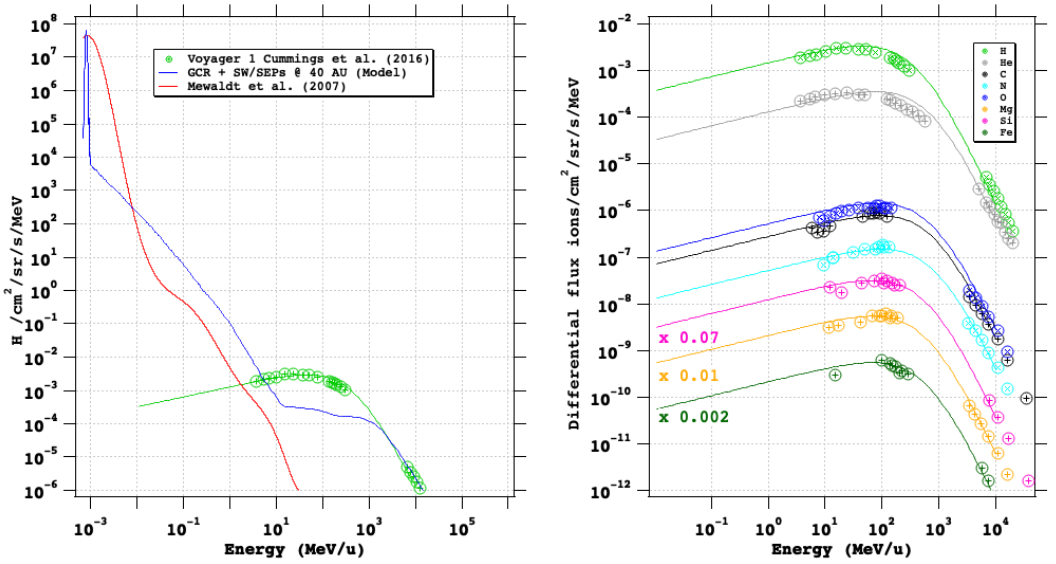

Figure 1: Left: The differential spectra of Solar Wind, Solar Energetic Particles and Galactic Cosmic Ray used in sputtering and doses calculations. Right: Voyager 1 data compared with the parametric law of Webber and Yushak (2003) calculated with C and E_0 values from Table 1 and the chemical abundances derived from Voyager 1 data at 80 MeV/u.

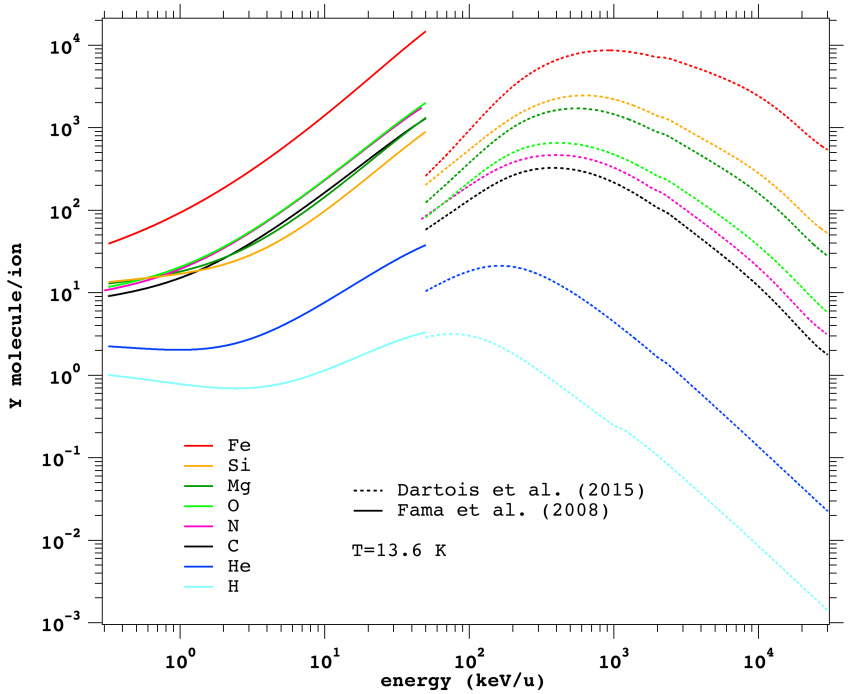

Figure 2: The sputtering yield of water ice calculated from Fama et al. (2008) at 13.6 K, compared with measurements from Brown et al. (1984) and Dartois et al. (2015). Note the mismatch at 50 keV/u, which likely points to an overestimation in the low energy range. At 50 keV/u and above, $S_e >> S_n$.

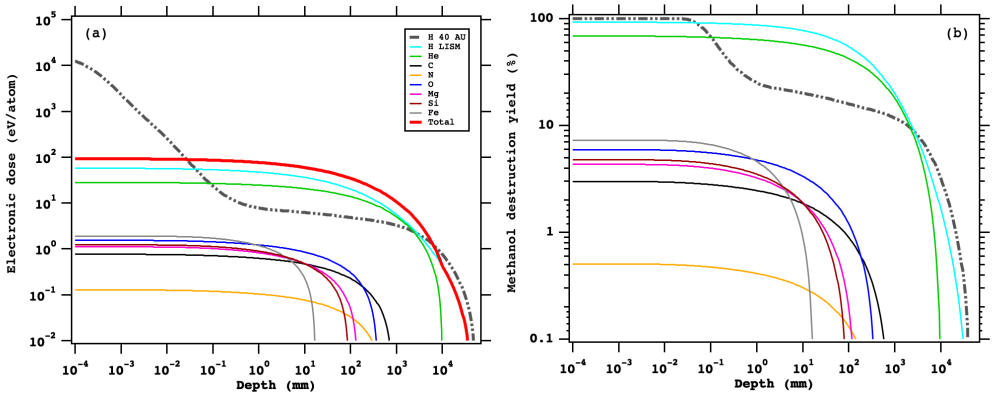

Figure 3: (a): Electronic dose deposited in Arrokoth's surface upon depth, for a LISM differential flux (solid lines) and protons differential flux at 40 au (mixed dotted line). (b): Destruction (breaking of the C-O bond) yield of methanol molecules (i.e., number of destroyed molecules divided by the initial number of molecules, multiplied by 100) using a revised destruction cross-section from de Barros et al. (2011). H and He are the main contributors to the dose, in term of intensity and depth.

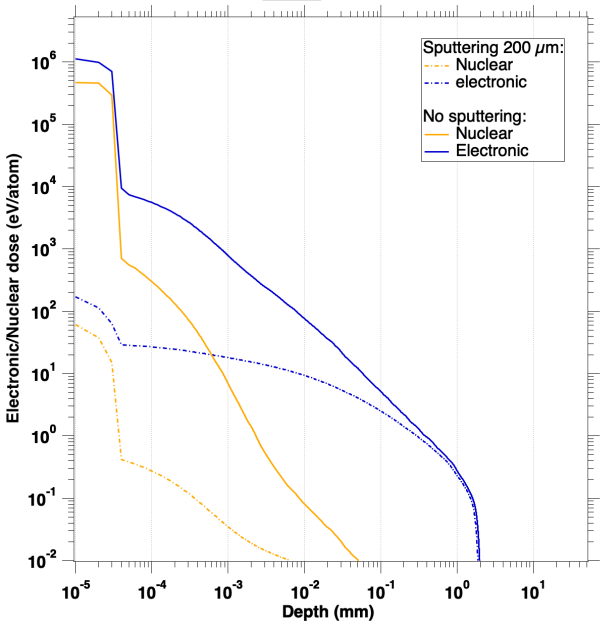

Figure 4: Electronic and nuclear doses deposited by Solar Wind ions at 44 au. Calculations were run without and with sputtering. The dose is significant in the first hundred of nm.

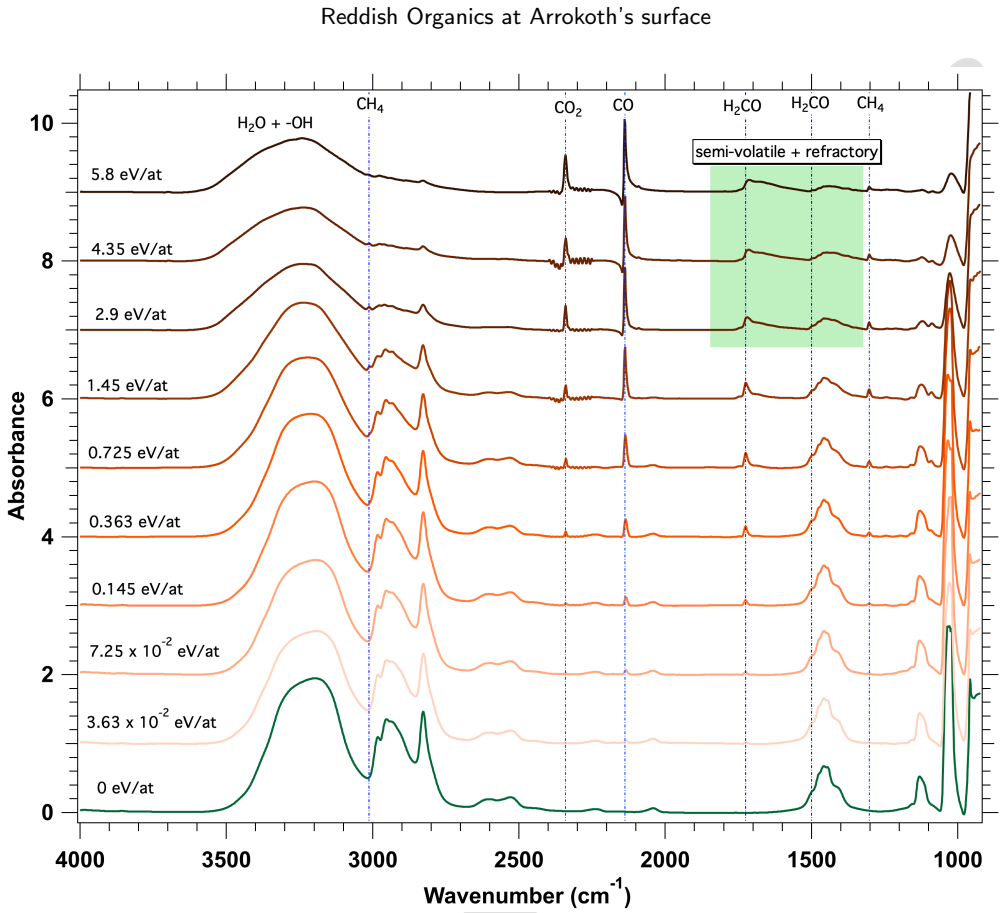

Figure 5: The evolution of methanol ice in experiment E_1. Signatures of organics appear around 1.45 eV.atom^{-1}.

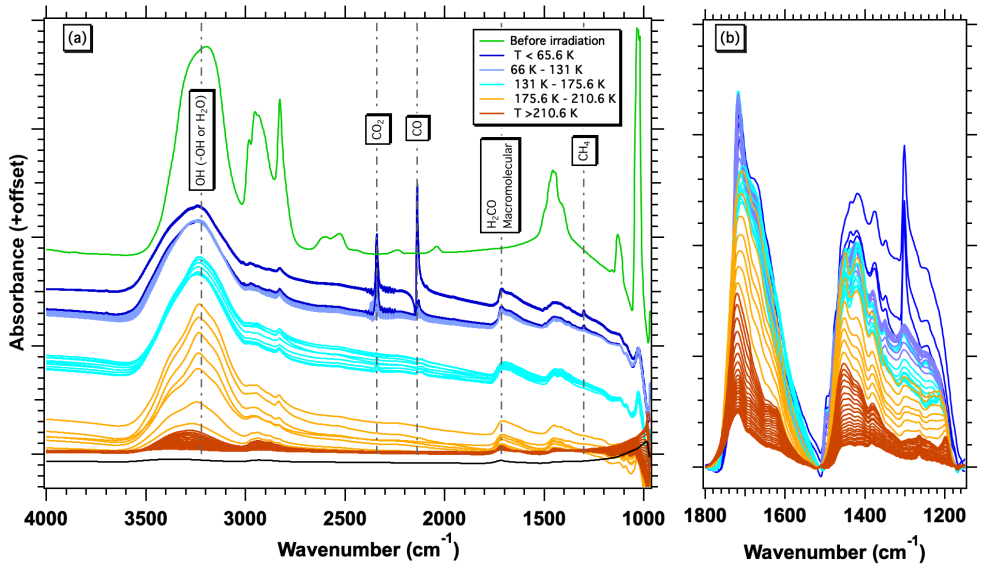

Figure 6: (a): Raw spectra of irradiated methanol film during thermal programmed desorption (experiment E1). (b): zoom on the organic bands with baseline correction.

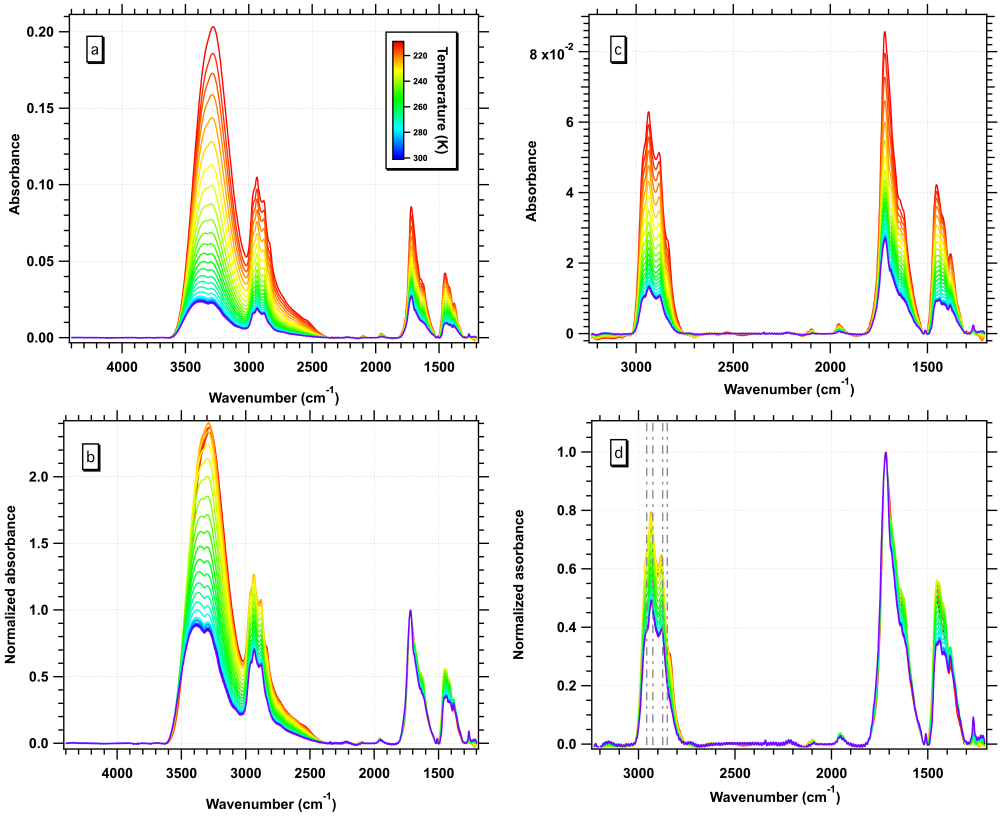

Figure 7: (a): Infrared spectra of organics during the Thermally Programmed Desorption sequence between 210 and 300 K. (b) Same with absorbance normalization at 1750 cm^{-1}. (c) Infrared spectra with a baseline correction in the region of the aliphatic band in the range 2800-3000 cm^{-1}. (d): Same with absorbance normalization at 1750 cm^{-1}.

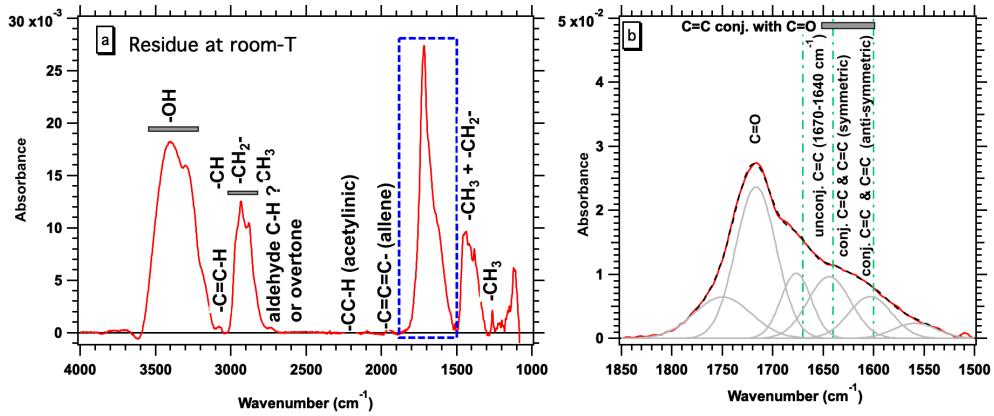

Figure 8: Bands assignment of the spectrum of the room temperature residue. (a): Full spectral range. (b): Blow out on the 1850-1500 cm^{-1}, which contains signatures of olefinic groups that control the absorption properties in the visible range.

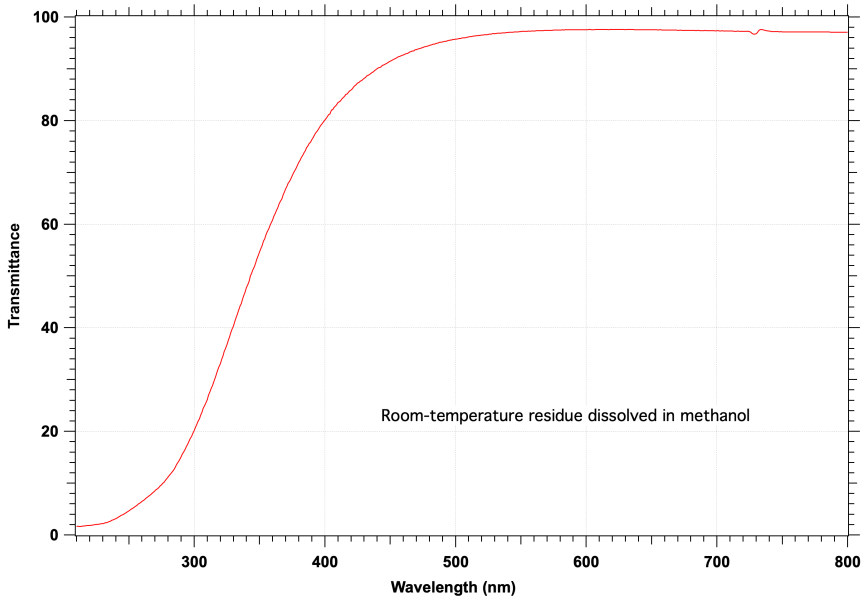

Figure 9: VUV absorption spectrum of the room temperature residue dissolved in methanol.

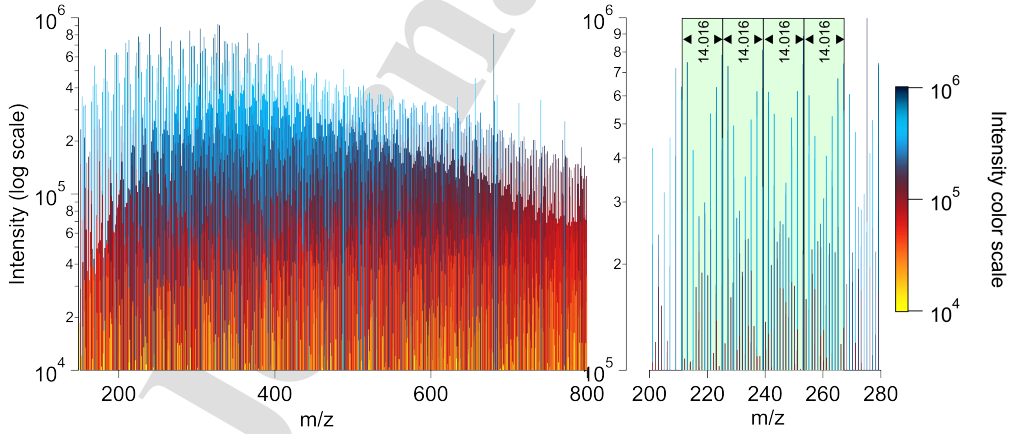

Figure 10: ESI mass spectra, with intensity color code in log scale. The right spectrum is a zoom between 200 and 280 Da as well as between 10^5 and 10^6 intensities. The large number of mass peaks at each nominal mass reflects the complexity of the sample.

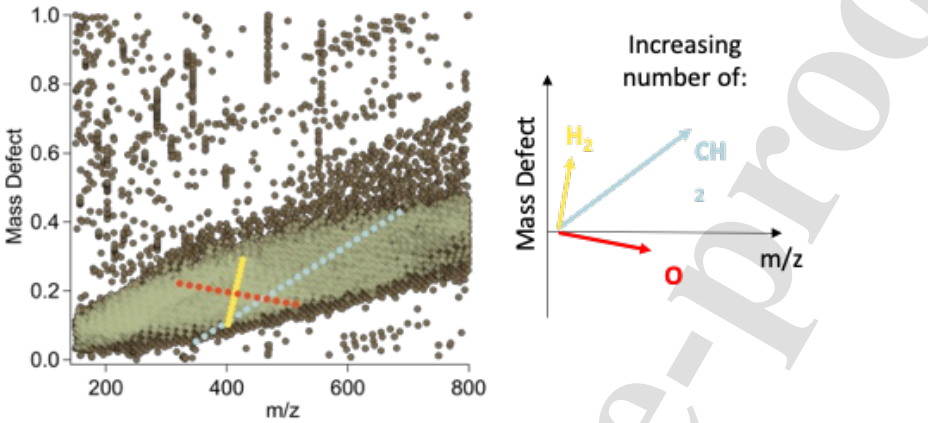

Figure 11: Mass defect versus mass diagram with three main directions being represented. The purple data points represent the final points assigned a stoichiometric formula. Other points are artifacts, as radiofrequency signals contamination (e.g. red area) or electronic noise (e.g. light blue area). The contribution of multicharged ions is negligible.

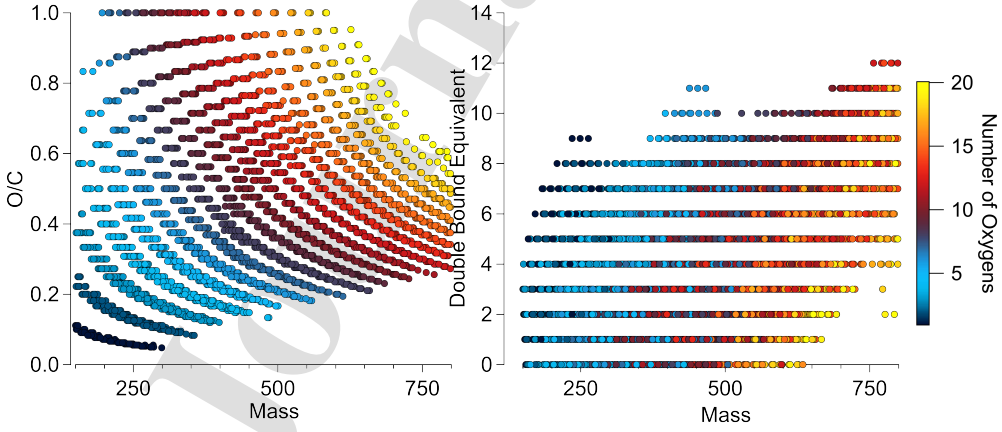

Figure 12: O/C and DBE versus mass representations, with the number of oxygens as colour code

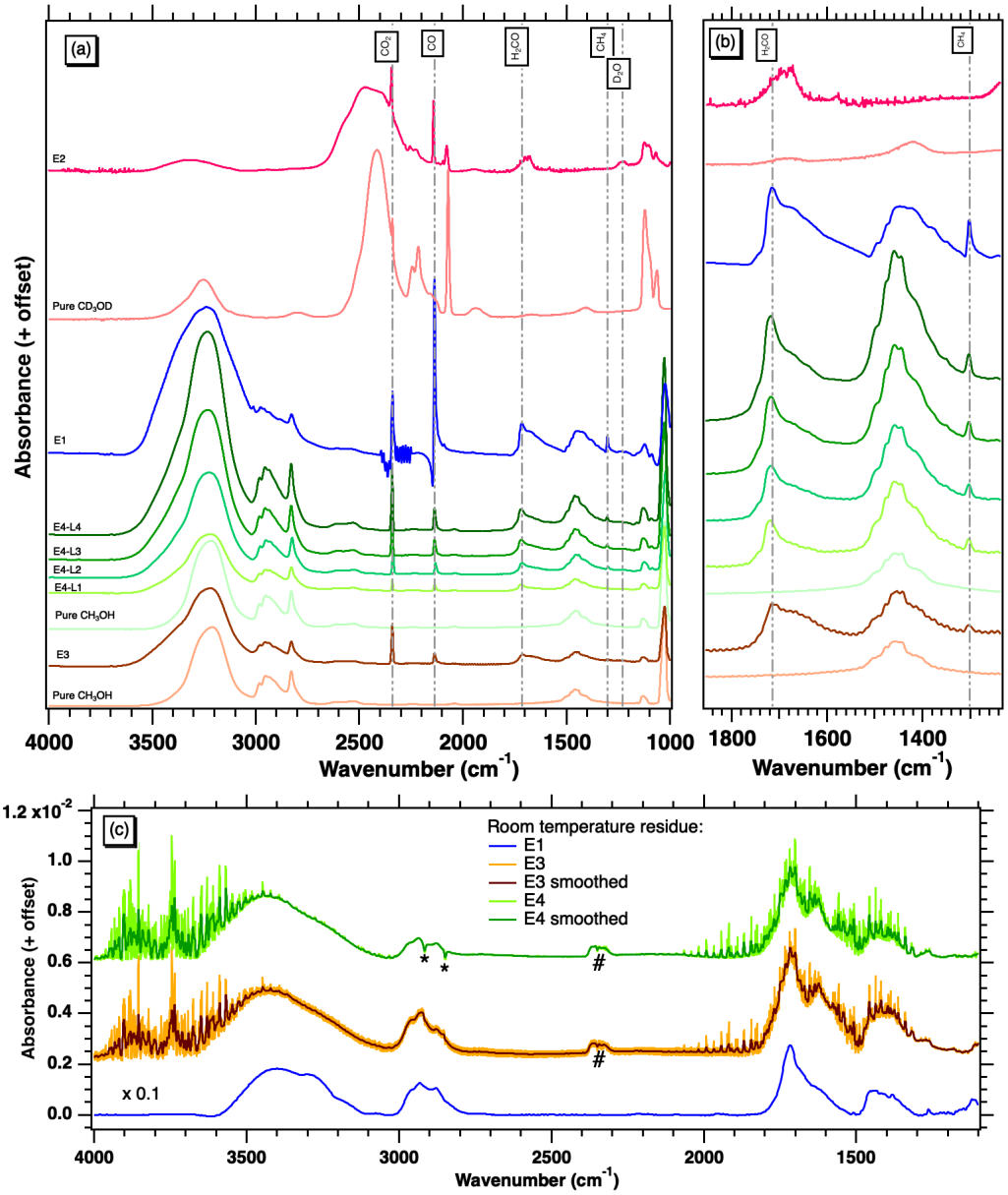

Figure 13: (a): Spectra of methanol films after irradiation for experiments E2, E3 and E4. The Li label refers to the layers from i=1 to 4 in experiment E4. (b): Blow up in the region of the organic bands. (c): Room temperature residues. *: artifact due to window pollution and background subtraction. ♯: incomplete correction of atmospheric CO_2.

Reddish Organics at Arrokoth's surface

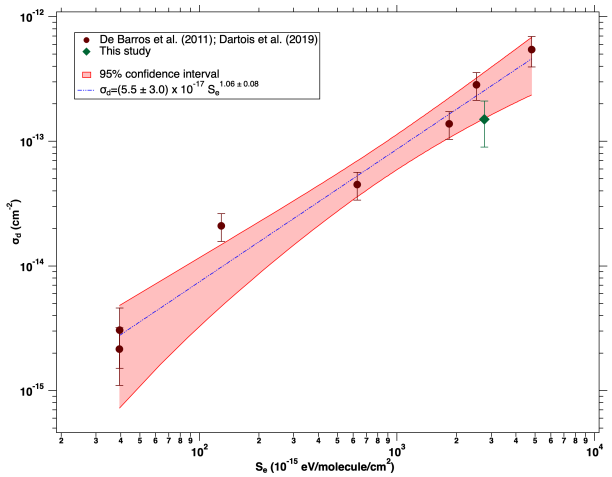

Figure 14: The destruction cross-section for CD_3OD derived from experiment E_2, compared with experimental data of earlier studies.

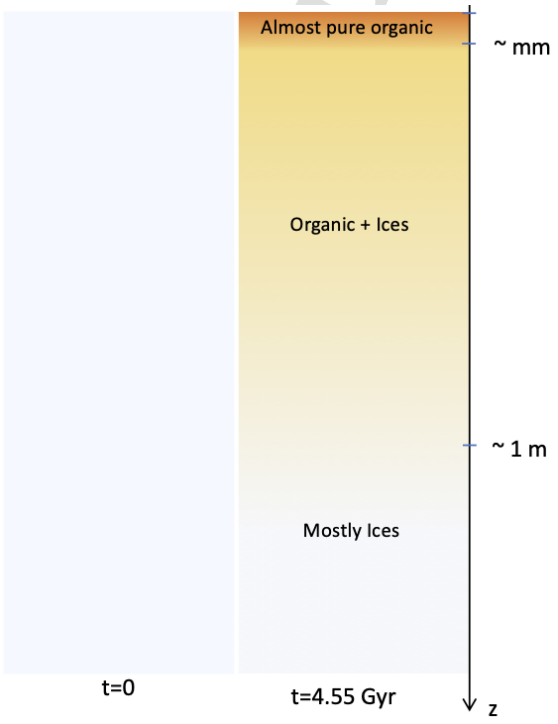

Figure 15: Distribution of organic radiolytic byproducts upon depth. The uppermost region of the surface is an almost pure organic crust, due to volatile removal by sputtering. The first meter region, where electronic dose is $> \sim 2$ eV.atom^{-1}, contains a significant abundance of organics. GCR protons goes down to several tens of meters, but produce there much less organic due to the lower dose.

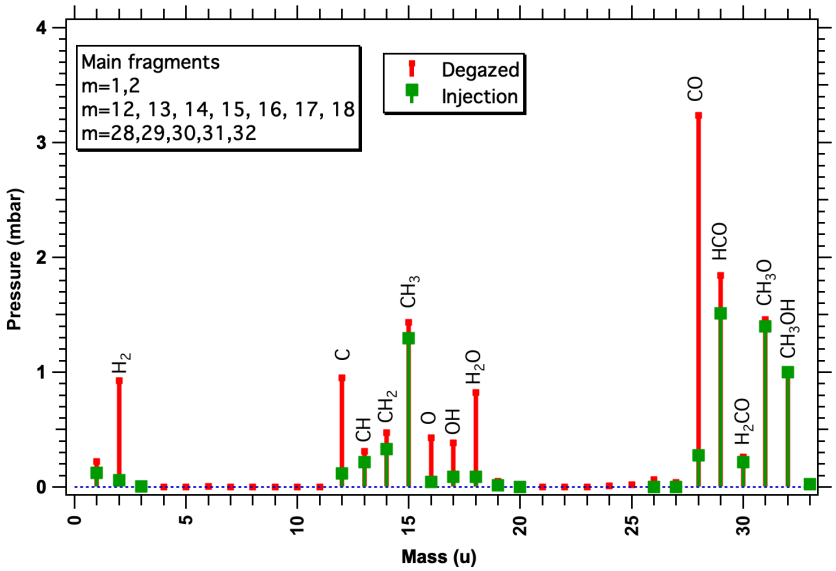

Figure 16: QMS spectra collected during injection (pure methanol) and during TPD.

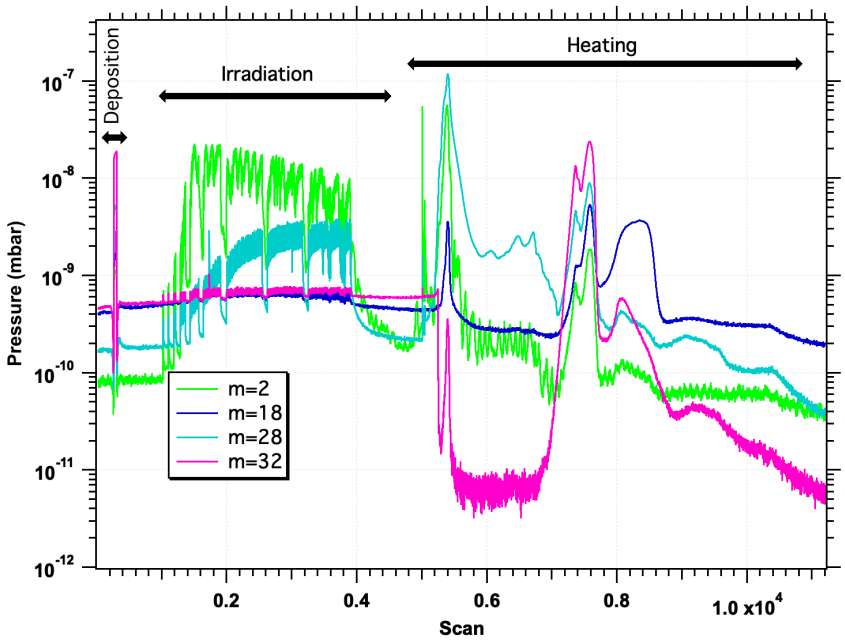

Figure 17: Peak intensity at m/z=2, 18, 28 and 32 during injection, irradiation and TPD.

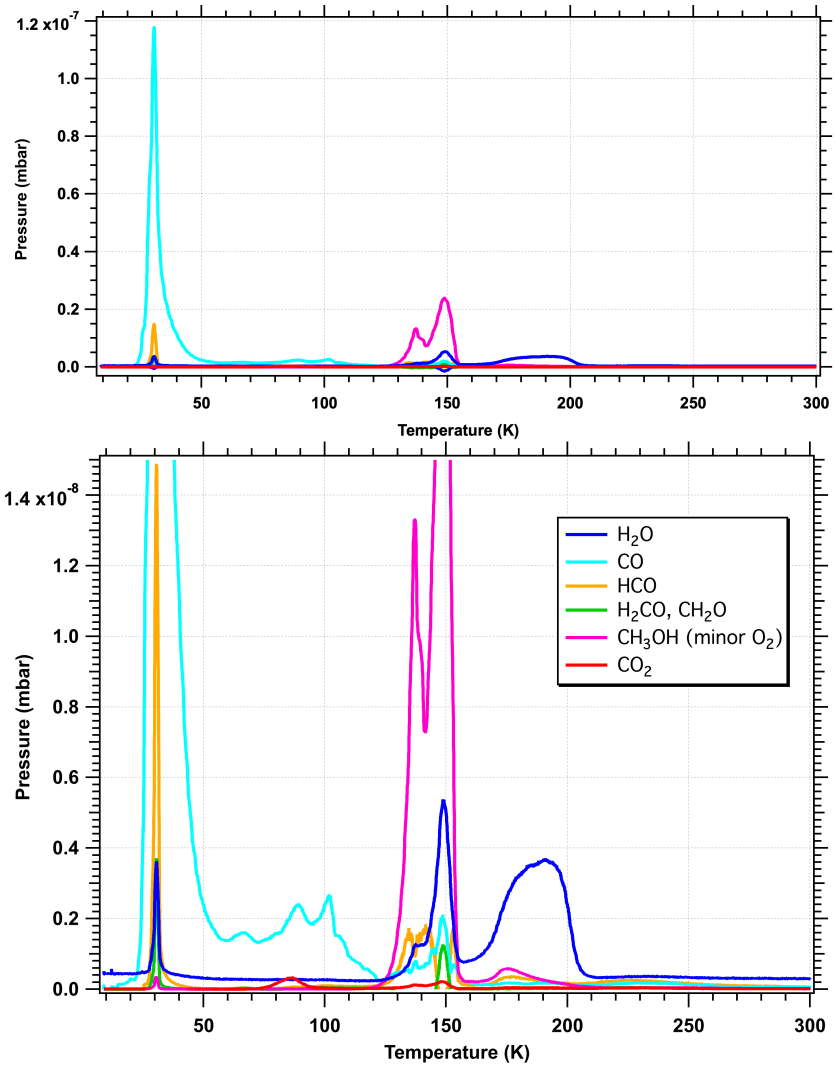

Figure 18: Top: The peak intensity of the main gaseous by-product after correction from CH_3OH contribution in the mass spectra, plotted against temperature. Bottom: same with magnification. No correction of the electron-impact cross sections and of the fragmentation patterns of the by-products were applied to the data.